Nano Research

ISSN 1998-0124 CN 11-5974/O4
https://doi.org/10.26599/NR.2026.94909245

Research Article

A tunable air-bubble microneedle system delivers gambogic acid for alleviating psoriasis-like skin inflammation

Huan Yang[1,§], Dandan Mi[1,§], Rujing Wang[2,§], Lan Zou[1], Yuyu Wei[1], Yan Tang[1], Yan Li[3], Wenwei Zuo[4], Sanjun Shi[1], Mengnan Zhao[1](✉)

[1] Chinese Medicine Germplasm Resources Innovation and Effective Uses Key Laboratory of Sichuan Province, School of Pharmacy, School of Modern Chinese Medicine Industry, Chengdu University of Traditional Chinese Medicine, Chengdu, China

[2] School of Basic Medical Sciences, Chengdu University of Traditional Chinese Medicine, Chengdu, China

[3] Chengdu Brilliant Pharmaceutical Co., Ltd, Chengdu, China

[4] Department of General Surgery, Hospital of Chengdu University of Traditional Chinese Medicine, Chengdu, China

[§] Huan Yang, Dandan Mi, and Rujing Wang contributed equally to this work.

Nano Res., **Just Accepted Manuscript** • https://doi.org/10.26599/NR.2026.94909245

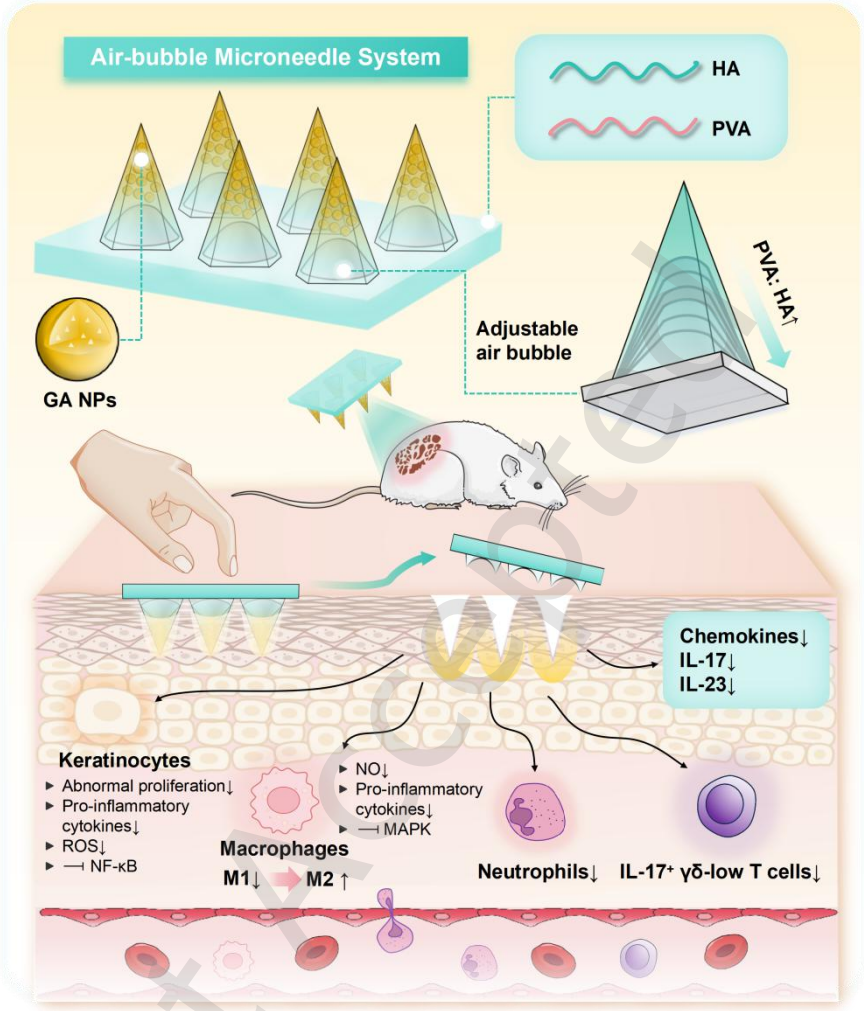
https://www.sciopen.com/journal/1998-0124 on Oct. 7, 2026

© The Authors(s)

Just Accepted

This is a "Just Accepted" manuscript, which has been examined by the peer-review process and has been accepted for publication. A "Just Accepted" manuscript is published online shortly after its acceptance,which is prior to technical editing and formatting and author proofing. Tsinghua University Press (TUP) provides "Just Accepted" as an optional and free service which allows authors to make their results available to the research community as soon as possible after acceptance. After a manuscript has been technically edited and formatted, and the page proofs have been corrected, it will be removed from the "Just Accepted" web site and published officially with volume and article number (e.g., *Nano Research*, **2025**, *18*, 94906990). Please note that technical editing may introduce minor changes to the manuscript text and/or graphics which may affect the content, and all legal disclaimers that apply to the journal pertain. In no event shall TUP be held responsible for errors or consequences arising from the use of any information contained in these "Just Accepted" manuscripts. To cite this anuscript please use its Digital Object Identifier (DOI®),which is identical for all formats of publication.

TABLE OF CONTENTS (TOC)



Schematic illustration of an air-bubble microneedle system loaded with gambogic acid nanoparticles for the treatment of psoriasis-like skin inflammation.

Just Accepted

Nano Research

Open Access

Research Article

A tunable air-bubble microneedle system delivers gambogic acid for alleviating psoriasis-like skin inflammation

Huan Yang[1,§], Dandan Mi[1, §], Rujing Wang[2,§], Lan Zou[1], Yuyu Wei[1], Yan Tang[1], Yan Li[3], Wenwei Zuo[4], Sanjun Shi[1], and Mengnan Zhao [1]

[1] *Chinese Medicine Germplasm Resources Innovation and Effective Uses Key Laboratory of Sichuan Province, School of Pharmacy, School of Modern Chinese Medicine Industry, Chengdu University of Traditional Chinese Medicine, Chengdu, China*
[2] *School of Basic Medical Sciences, Chengdu University of Traditional Chinese Medicine, Chengdu, China*
[3] *Chengdu Brilliant Pharmaceutical Co., Ltd, Chengdu, China*
[4] *Department of General Surgery, Hospital of Chengdu University of Traditional Chinese Medicine, Chengdu, China*
[§] *Huan Yang, Dandan Mi, and Rujing Wang contributed equally to this work.*

Received: 13 August 2026; **Revised:** 2 October 2026; **Accepted:** 7 October 2026

Address correspondence to zhaomengnan@cdutcm.edu.cn

Cite this article: *Nano Research*, 2026, 19, 94909245 https://doi.org/10.26599/NR.2026.94909245

ABSTRACT: Psoriasis is a chronic inflammatory skin disease driven by keratinocyte hyperproliferation and excessive cytokine secretion. Here, we explored the therapeutic potential of Gambogic acid (GA), a natural compound whose application in psoriasis has received limited attention despite its great potential. To enhance drug penetration into psoriatic lesions, GA was encapsulated within poly (lactic-co-glycolic acid) (PLGA) nanoparticles and loaded onto microneedle tips fabricated from a poly (vinyl alcohol) (PVA)/hyaluronic acid (HA) blend. Interestingly, we observed that air bubbles could form during the fabrication process and that the bubble size was readily tunable simply by varying the PVA-to-HA ratio—a phenomenon barely reported before. We systematically analyzed the factors modulating bubble size and identified the thickness of dried polymer films as the dominant factor governing final bubble dimensions, and such tunable bubble volumes are capable of altering the dissolution duration of needle tips. Furthermore, we demonstrated that GA exerts anti-psoriatic effects by suppressing TWEAK- and TNF- α- induced hyperproliferation of HaCaT cells, while also inhibiting the NF- κB pathway in these cells and modulating inflammatory responses in macrophages via the MAPK pathway. *In vivo* studies showed that GA-loaded microneedle patches significantly alleviated psoriasis-like skin inflammation in mice by inhibiting keratinocyte hyperproliferation, modulating macrophage polarization, reducing neutrophils and IL-17+ γδ-low T cells, and downregulating key inflammatory cytokines. Collectively, this study not only provides a systematic mechanistic and pharmacodynamic foundation for further application of GA in psoriasis treatment, but also establishes a facile method for fabricating air-bubble-structured microneedles to enhance transdermal delivery of natural compounds.

KEYWORDS: air bubble-structured microneedle, gambogic acid, nanoparticle, psoriasis, inflammation.

Just Accepted

1 Introduction

As a prevalent chronic papulosquamous dermatosis, psoriasis occurs globally, manifests at any age, and entails a substantial socioeconomic and personal burden[1]. Pathologically, it is characterized by acanthosis, hyperkeratosis, dermal hypervascularity, and dense infiltration of immune cells in the dermis[2]. Mechanistically, keratinocytes play a central role in amplifying psoriatic inflammation by secreting proinflammatory cytokines in response to environmental triggers[3-5]. A significant challenge in current psoriasis treatment, including immunosuppressants, biologics, and small-molecule drugs, is the variable patient response, which manifests as either primary or secondary non-response. Furthermore, the long-term safety profiles of these treatments remain a major concern. Given the chronic and recurrent nature of the disease, these limitations underscore the urgent need to identify novel therapeutic molecules[4].

Natural products, particularly xanthones, exhibit notable advantages in the treatment of skin inflammatory diseases due to their antioxidant and anti-inflammatory profiles[6]. Gambogic acid (GA), a naturally occurring polyprenylated xanthone isolated from the dry gamboge resin of *Garcinia hanburyi*, exhibits chemical stability and favorable biosafety (validated in phase IIa trials)[7]. Mechanistically, GA exerts its biological effects via the activation of the Nrf2 signaling pathway and the inhibition of NF-κB[8, 9]. Although preclinical studies have shown its efficacy in arthritis, kidney injury, and cancer models[10-12], limited studies have explored its therapeutic potential against psoriasis, and underlying mechanisms requiring further elucidation[13].

For dermatological conditions such as psoriasis, transdermal drug delivery is often the preferred route of administration. Typically, the molecular weight of drugs commonly used for transdermal delivery falls within a relatively low range, generally below 500 Da, as this molecular weight range is more conducive to penetrating the skin's stratum corneum barrier. However, the molecular weight of GA (~628 Da) exceeds the conventional threshold for efficient transdermal delivery[14-16]. Given the challenge of efficient transdermal delivery of drugs with poor transdermal permeability, microneedle technology emerges as a promising solution[17-19]. Microneedles comprise micrometre-scale arrays that pierce the stratum corneum to enable minimally invasive drug administration[20, 21]. They have demonstrated high efficiency in delivering a diverse array of therapeutics, ranging from small-molecular-weight drugs[22] to complex biological entities such as proteins[23, 24], nucleic acids[25, 26], nanoscale carriers[27], viral vectors[28], and extracellular vesicles[22, 29]. However, in continuous tip-backing microneedles, the difficulty in judging tip dissolution time often leads to inconsistent dose delivery[30]. Air-bubble integrated microneedles, featuring air gaps between each needle and the patch backing, were recently developed to address these issues. The microneedle array can detach from the backing quickly and easily once inserted into the skin. This feature eliminates uncertain dissolution intervals and thereby guarantees precise and uniform transdermal drug delivery.

This study presents a novel air-bubble microneedle patch integrated with GA-loaded poly (lactic-co-glycolic acid) (PLGA) nanoparticles for psoriasis treatment, in which tunable bubble volumes modulate needle-tip dissolution time (Scheme 1). Notably, the bubble size of these (vinyl alcohol) (PVA)/hyaluronic acid (HA) microneedles could be tailored simply by adjusting the PVA-to-HA ratio. The factors influencing bubble size were systematically analyzed. We then verified that GA inhibited HaCaT cell and macrophage inflammation through the NF-κB and MAPK pathways, respectively. *In vivo*, GA-loaded microneedle modulated the skin immune microenvironment by reducing M1 macrophages, elevating M2 macrophages, decreasing neutrophils and IL-17$^+$ γδ-low T cells, while downregulating gene expression of key inflammatory cytokines including *Il-17*, *Ccl5*, *Ccl20*, and *Il-23*. This study systematically elucidated the immunomodulatory mechanisms of GA in psoriasis while developing an air-bubble microneedle system for its topical delivery. Together, these findings validate GA as a mechanistically defined anti-psoriatic agent and offer a tunable microneedle platform that can be adapted for other small-molecule therapeutics.

2. Materials and methods

2.1 Materials

Polyvinyl alcohol (PVA, Mw 30000-70,000) was purchased from Beyotime Biotechnology. Hyaluronic acid (HA, Mw100,000-200,000) was purchased from Shanghai Yien Chemical Technology Co., Ltd. Poly (lactic-co-glycolic acid) (PLGA, 50:50) was purchased from Evonik Investment Co., Ltd. (China). Gambogic acid (GA) was purchased from Chengdu Phytomark Chemical Pure Biotechnology Co., Ltd. 4% paraformaldehyde was purchased from Wuhan Servicebio Technology Co., Ltd.

The β-Actin rabbit polyclonal antibody was purchased from Wuhan Servicebio Technology Co., Ltd. Tubulin was purchased from HuaBio. The NF-κB p65 antibody was purchased from Beyotime Biotechnology. Antibodies against IκB, p-IκB, Erk, p-Erk, and p38 were purchased from Abmart Co., Ltd. (Shanghai, China). Antibodies against IL-23, iNOS, and p-p38 were purchased from Wanlei Life Sciences Co., Ltd. (Shenyang, China). 5% imiquimod cream was purchased from Sichuan Med-Shine Pharmaceutical Co., Ltd.

2.2 Cell culture

The human keratinocyte cell line (HaCaT) was purchased from Procell Life Science & Technology Co., Ltd. (Wuhan, China). Cells were cultured in Dulbecco's modified Eagle's medium (DMEM, Gibco) supplemented with 15% fetal bovine serum (FBS, Immocell) and 1% penicillin-streptomycin under a humidified atmosphere containing 5% CO2 at 37°C.

RAW264.7 cells were purchased from the Shanghai Cell Bank, Chinese Academy of Sciences. Cells were cultured in DMEM supplemented with 10% FBS and 1% penicillin-streptomycin under the same incubation conditions (37°C, 5% CO2).

Just Accepted

2.3 Animals

Female BALB/c mice (6-8 weeks) were obtained from SPF Biotechnology (Beijing, China). The mice were housed in a standard environment. Following a one-week acclimation period, all experimental procedures were performed in strict accordance with the ethics Committee guidelines of Chengdu University of Traditional Chinese Medicine.

2.4 Cell viability assay

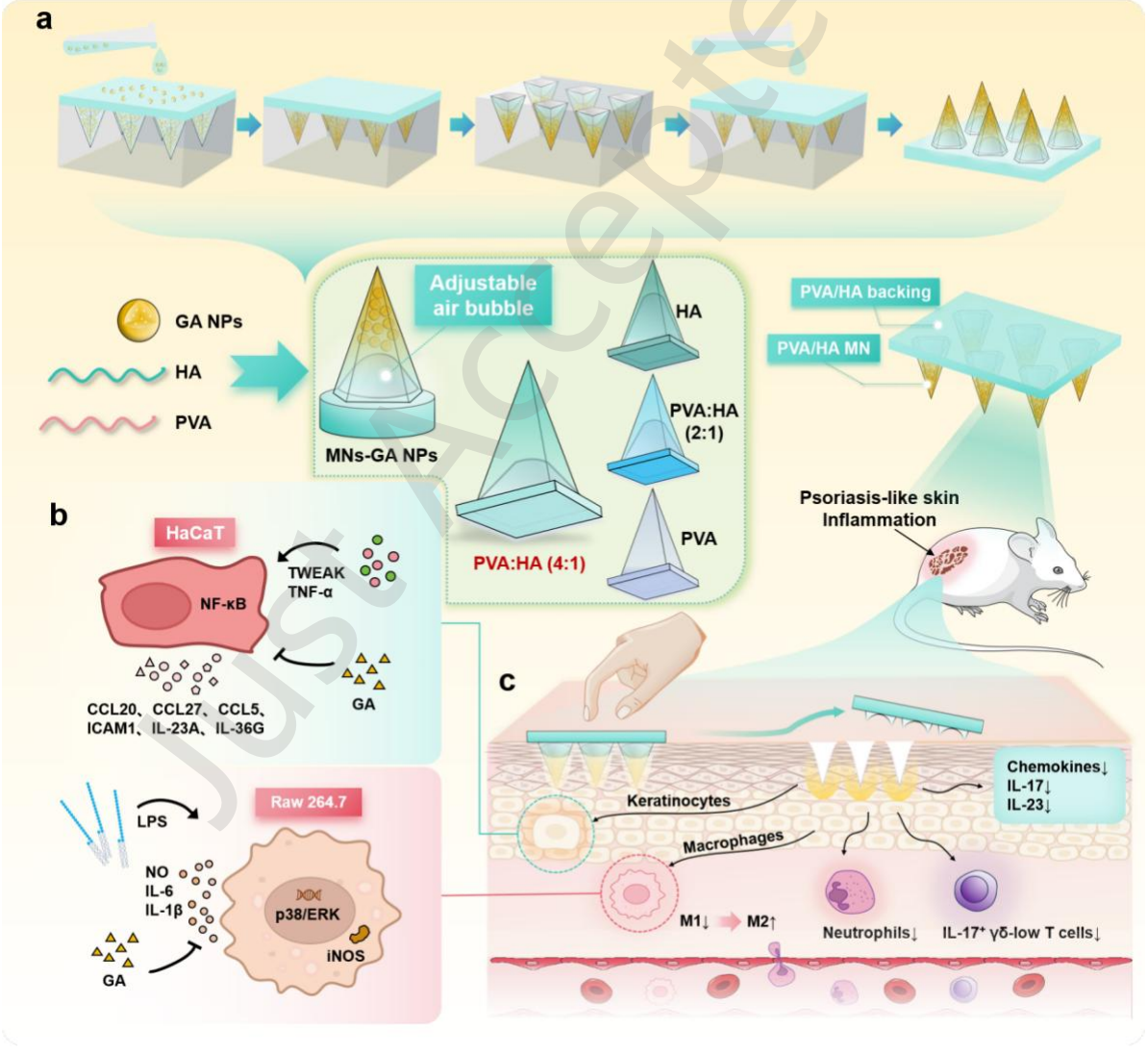
HaCaT cells and RAW264.7 cells were seeded into a 96-well plate and cultured overnight at 37°C with 5% CO2. The cells were treated with cytokines or GA at different concentrations for another 48 h. Subsequently, 10 μL of CCK-8 solution was added to each well, followed by incubation at 37°C in the dark for 1 h. The absorbance was measured at 450 nm using a microplate reader to evaluate cell viability.

2.5 EdU assay

HaCaT cells were seeded into 12-well plates and cultured overnight. After cytokine stimulation, fresh medium or GA at different concentrations was added 2 h later, and the cells were incubated for 48 h. EdU staining was performed according to the instructions of the BeyoClick™ EdU Cell Proliferation Kit with Alexa Fluor 647. The samples were analyzed using FACSVerse flow cytometer (BD, USA) and Fluorescence microscope (Leica, Germany).

2.6 Cell scratch assay

HaCaT cells were seeded into 12-well plates and cultured overnight. A straight scratch was created in the confluent cell monolayer using a 200 μL pipette tip. The cells were then treated with control medium or medium containing TWEAK and TNF-α. After 2 h, control medium or GA at different concentrations was added, and the cells were incubated for 48 h. Images were captured at 0, 24, and 48 h after scratching. The wound closure was analyzed using ImageJ software.



Scheme 1 Schematic illustration of an air-bubble microneedle system loaded with gambogic acid nanoparticles for the treatment of psoriasis-like skin inflammation.

2.7 Transcriptomics analysis

HaCaT cells were seeded in 12-well plates and cultured overnight. After cytokine stimulation for 2 h, the cells were treated with GA (0.5 and 1 μM) for 24 h. Total RNA was extracted, and libraries were constructed. Differentially expressed genes were identified using the featureCounts tools in the Subread package. GO and KEGG enrichment

Just Accepted

analyses were performed using clusterProfiler.

2.8 NF-κB nuclear translocation assay

HaCaT cells were seeded onto coverslips and treated with cytokines or GA at different concentrations. After fixation and immunofluorescence staining with an NF-κB p65 antibody and Cy3-conjugated secondary antibody, nuclei were counterstained with DAPI. NF-κB nuclear translocation was observed using a fluorescence microscope (Leica, Germany).

2.9 Western Blot analysis

HaCaT cells were seeded into 6-well plates and treated as indicated. Total proteins were extracted using RIPA lysis buffer containing PMSF and phosphatase inhibitors (Epizyme, China). Protein concentrations were determined using a BCA assay kit (Beyotime, Shanghai). Equal amounts of protein were separated by SDS-PAGE, transferred onto PVDF membranes (Roche, Germany), and blocked. The membranes were incubated with primary antibodies overnight at 4 °C, followed by secondary antibody incubation. Protein bands were detected using an OI 600 automatic chemiluminescence imaging system (BIO-OI, China).

2.10 Real Time q-PCR

HaCaT cells or RAW264.7 cells were seeded into 12-well plates and incubated overnight in a culture incubator until cells were fully adherent. After the cells were treated with cytokines and GA for 24 h, total RNA was extracted using RNAex Pro reagent (Accurate Biology, China). Subsequently, cDNA was synthesized via reverse transcription using the EVO M-MLV RT kit (Accurate Biology, China). Finally, qPCR amplification was conducted using the SYBR Green Premix Pro Taq HS qPCR kit (Accurate Biology) on a Gentier 48E/48R qPCR system (Tianlong Technology, China). Primer sequences are listed in Supplementary Table S2 and Table S3. Relative gene expression levels were calculated using the $2^{(-\Delta\Delta Ct)}$ method.

2.11 Cell uptake assay

Coumarin 6 (C6) -loaded PLGA nanoparticles were used as a fluorescent probe to mimic water-insoluble GA. HaCaT cells were treated with free C6 or C6-loaded nanoparticles for 2 h. Cellular uptake was analyzed by flow cytometry and visualized using confocal laser scanning microscopy (CLSM, FLUOVIEW FV4000, Evident Scientific, Tokyo, Japan).

2.12 NO detection assay

The LPS- induced RAW264.7 cells inflammation model is a widely used in vitro screening tool for anti- inflammatory studies in psoriasis. It was used for the preliminary evaluation of GA activity, and the in vivo efficacy was subsequently confirmed in the IMQ mouse model. RAW264.7 cells were seeded into 6-well plates and treated with GA (0.1 or 0.2 μM) for 1 h, followed by stimulation with LPS (1 μg/mL) for 24 h. The culture supernatants were collected, and NO production was measured using the Griess reagent assay (Beyotime, Shanghai). Absorbance was measured at 540 nm using a microplate reader.

2.13 Preparation and characterization of GA NPs

60 mg of PLGA and 6 mg of GA were dissolved in 2 mL of dichloromethane (DCM), followed by addition of 4.5 mL of 3% PVA aqueous solution. The mixture was emulsified by vortexing and sonicated using an ultrasonic cell disruptor (50 W, 5 s × 5 s, 10 min). DCM was removed by rotary evaporation at room temperature. The resulting suspension was diluted, filtered and centrifuged (12,000 rpm, 40 min, 4°C). The precipitate was washed twice by centrifugation and resuspended in deionized (DI) water to obtain GA NPs. The particle size, polydispersity index (PDI), and Zeta potential of GA NPs were measured using a BeNano 90 Zeta nanoparticle analyzer (Bettersize Instrument, China). The morphology was characterized by transmission electron microscopy (TEM). The encapsulation efficiency and drug loading were determined by high-performance liquid chromatography (HPLC) using a Diamonsil C_{18} column (250 × 4.6 mm, 5 μm).

2.14 Fabrication of MN Patches

Air-bubble microneedles (MN) patches were fabricated using a two-step casting method. The microneedle tips were filled under vacuum (0.1 MPa) for 15–40 min. After the excess solution was removed, and the molds were filled with the backing layer solution. The MN patches were dried at 60°C for 4 h, demolded, and stored in a desiccator at room temperature. GA NP-loaded soluble MNs were prepared by replacing the DI water with GA NPs solution. Fluorescently labeled MNs were fabricated using DiD-labeled PLGA NPs or Rhodamine B (RhB) instead of GA NPs.

2.15 Characterization and mechanical properties of MNs patches

The rheological properties of the PVA/HA microneedle matrix solution were analyzed using a rheometer at 25°C with shear rate ramped from 0.1 to 100 s-1. The morphology of MN patches was characterized by optical microscopy, scanning electron microscopy (SEM), and CLSM (Evident Scientific, Japan).

The mechanical properties of GA NPs MNs were evaluated using a universal testing machine (SANS-UTM-510, China). Dried MN patches were placed on the testing stage with the needle tips facing upward and compressed vertically at a speed of 1.2 mm/min. The mechanical strength was analyzed based on the stress-displacement curves.

Dried MN patches were immediately weighed (W_0) and placed under ambient conditions. The samples were weighed at predetermined time points (3, 6, 9, 12 and 24 h). The moisture absorption rate was calculated based on the weight change.

2.16 *In vitro* dissolution performance and skin penetration ability of MN patches

A single row of MNs was fixed onto a 6 cm culture dish and immersed in PBS to evaluate dissolution behavior. The morphology of MNs at predetermined time points was observed by electron microscopy. To evaluate the skin penetration capability of the microneedle patches, patches loaded with DiD- labeled NPs were used. The patches were applied to the porcine skin for a predetermined duration. After removal, the penetration of the microneedles was

Just Accepted

analyzed using confocal microscopy.

2.17 GA release from MN patches

The *in vitro* release of GA from MN patches was evaluated by immersing the patches in 1 mL of PBS containing 0.5% (v/v) Tween 80 at 37°C under shaking (100 rpm). At predetermined time intervals, 1 mL of the released medium was collected and replaced with an equal volume of fresh medium. The collected samples were analyzed by HPLC to determine GA release.

The transdermal delivery of GA was evaluated using a Franz diffusion cell system with a diffusion area of approximately 0.64 cm^2. After MN insertion into excised mouse skin, the skin samples were mounted between the donor and receptor chambers. The receptor chamber was filled with 5 mL of PBS containing 0.5% (v/v) Tween 80 and maintained at 32 ± 1°C with continuous stirring (300 rpm). At predetermined intervals, samples were collected and replaced with fresh medium. GA content was quantified by HPLC.

2.18 *In vivo* pharmacodynamic study

Female BALB/c mice were used to establish an imiquimod (IMQ)-induced psoriasis-like model. After one week of acclimatization, mice were randomly divided into seven groups (n = 6): Normal, Model, Blank MNs, MNs- NPs, low-dose MNs-GA NPs (1 mg/kg), high-dose MNs-GA NPs (2 mg/kg), and dexamethasone (Dex) groups. The dorsal hair was removed, and the skin was allowed to recover for 1 day. Except for the Normal group, mice were treated with 62.5 mg of 5% IMQ cream daily for 5 consecutive days to induce psoriasis-like inflammation. Starting from day 2 after IMQ application, different treatments were administered daily according to the assigned groups. Specifically, mice in the MN patch groups (Blank MNs, MNs- NPs, low- dose, and high- dose MNs- GA NPs) received one patch per day, while the Dex group received 70 mg of dexamethasone cream (equivalent to 0.05 mg of dexamethasone) applied topically to the bare dorsal skin daily.

Body weight and psoriasis severity scores were recorded daily. Disease severity was evaluated using the PASI scoring system, including erythema, skin thickening, and scaling (0–4 points for each parameter). On day 6, mice were sacrificed, and dorsal skin tissues were collected for histological and immunological analyses. Tissue sections were stained with hematoxylin and eosin (H&E). Immunohistochemistry (IHC) was performed to detect Ki67 expression, while immunofluorescence (IF) staining was conducted to evaluate IL-17 and IL-23 expression. Histological images were quantified using ImageJ software.

The effect of MNs-GA NPs patches on immune cells in psoriasis lesions was evaluated by flow cytometry. Skin tissues were dissociated into single-cell suspensions and stained with fluorescent antibodies after Fc receptor blocking. T cells were identified using anti-CD3, anti-γδ-TCR, and anti-CCR6 antibodies; neutrophils were characterized using anti-CD11b and anti-Ly6G antibodies; M1 macrophages were identified by CD11b, F4/80 and CD86 expression; and M2 macrophages were identified by CD11b, F4/80 and Arg1 expression. After staining, cells were analyzed using FACSVerse flow cytometer (BD, USA).

2.19 Statistical analysis

All data are presented as mean ± standard deviation (SD). Statistical analysis was performed using GraphPad Prism 9.0 software (GraphPad Software, USA). For comparisons between two groups, unpaired Student's t-test was used. For comparisons among three or more groups, one-way/two-way analysis of variance (ANOVA) was performed, Significance is shown on graphs as $*p < 0.05$, $**p < 0.01$, $***p < 0.001$.

3. Results and discussion

3.1 GA Inhibited Abnormal HaCaT Cell Proliferation Stimulated by TNF-α Alone or in Combination with TWEAK

TWEAK protein, a member of the tumor necrosis factor (TNF) superfamily, is a cytokine that serves as a weak inducer of apoptosis. It displayed strong synergism with TNF in up-regulating messenger RNA for many psoriasis-associated genes in human keratinocytes[3]. Therefore, we sought to evaluate the impact of GA to inhibit the proliferation of HaCaT cells, stimulated by TNF-α alone or in combination with TWEAK. First, we examined the effects of TNF-α alone on HaCaT cells. The optimal concentration of TNF-α was evaluated by CCK-8 and EDU assays. 60 ng/mL TNF-α significantly promoted the proliferation of HaCaT cells, while at higher concentrations, the cell viability and proliferation levels decreased which might be due to the cytotoxicity of TNF-α (Fig. 1(a) and S1(a)-(b)). Subsequently, an EdU assay was performed to further investigate the inhibitory effect of GA on TNF-α-stimulated cell proliferation (Fig. 1(b)). Fluorescence images and flow cytometry results showed that even at concentrations exhibiting negligible cytotoxicity (0.5, 0.75 and 1 μM) (Fig. 1(c)), GA could still markedly inhibit the proliferation of HaCaT cells (Fig. 1(d)-(f) and S1(c)-(d)).

When TWEAK and TNF-α are used in combination, TNF-α is typically applied at lower concentrations[3]. Thus, we further optimized the concentrations of the co-administration of these two cytokines (Fig. 1(g) and S2(a)-(b)). For downstream pathway analysis, we aimed to observe the trend of signaling changes rather than the maximal effect; 20 ng/mL TWEAK combined with TNF- α was sufficient to induce a significant proliferative response. We selected concentrations that were relatively low but have the most obvious stimulating effect for subsequent experiments (20 ng/mL TWEAK and 10 ng/mL TNF-α) (Fig. 1(h)). Then, we examined the impact of GA (0.5, 0.75 and 1 μM) exposure on cell viability (Fig. 1(i)). The results of the EdU assay, analyzed via fluorescence microscope (Fig. 1(j) and S2(c)) and flow cytometry (Fig. 1(k)-(l) and S2(d)), revealed that GA effectively inhibited the abnormal proliferation of HaCaT cells stimulated by two cytokines. Similarly, cell scratch assay results also indicated that GA has the potential to inhibit TWEAK and TNF-α-induced abnormal migration of HaCaT cells *in vitro* (Fig. S3).

3.2 GA Modulates Inflammatory Pathways & Pro-Inflammatory Genes in TNF-α/TWEAK-Stimulated HaCaT Cells

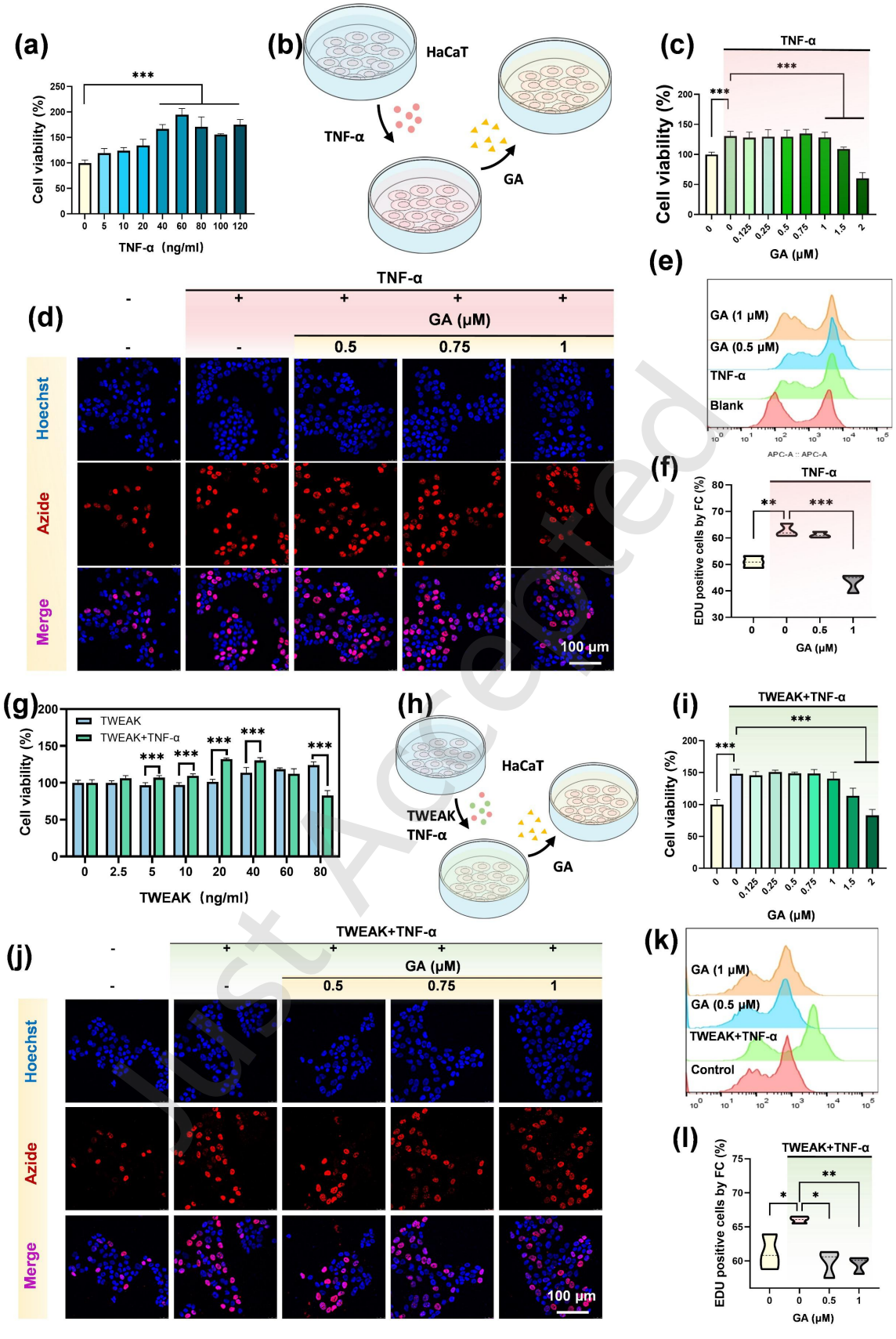
Just Accepted

To further explore the mechanism by which GA inhibits the abnormal proliferation of HaCaT cells stimulated by TNF-α and TWEAK, we conducted a transcriptomics analysis (Fig. 2(a)). Results from PCA analysis indicated significant differences between groups, good intra-group reproducibility, and acceptable quality control, allowing for further analysis (Fig. 2(b)). Relative to the control group, the modeling group showed upregulation of genes contributing to pro-inflammatory responses, such as *CCL5*, *ICAM1*, *IL23A*, *CXCL1*, and *CXCL8* (Fig. 2(c)). In turn, compared with the modeling group, the treatment group exhibited downregulation of *CCL5*, *CXCL1*, and *CXCL8* (Fig. 2(d)). Figure 2(e) displayed the overlap of differentially expressed genes between two comparisons. The 516 overlapping genes highlight a core set regulated by both cytokines' stimulation and GA intervention. Figure 2(f) visualized expression patterns of key genes like *CXCL1* and *CCL5* across Blank, TWEAK- and TNF-α-treated, and GA-intervened groups. KEGG pathway enrichment for genes upregulated in the Model group versus Blank group indicates pathways like "NF-κB signaling pathway" and "Cytokine-cytokine receptor interaction" are prominently enriched, reflecting inflammatory and immune activation (Fig. 2(g)). The genes downregulated in the GA-intervened group (Model+GA) versus Model group comparison were mostly involved in pathways such as "TNF signaling pathway" and "NF-κB signaling pathway" (Fig. 2(h)). Gene Ontology (GO) enrichment for genes downregulated in the Model+GA group vs Model group indicates high enrichment in immune-related biological processes, and coordinated regulation across cytokine activity-related cellular components (Fig. 2(i)). Psoriasis is a chronic inflammatory skin disease characterized by increased inflammatory cell infiltration and secretion of related inflammatory factors[31]. The above transcriptomic analyses reveal that GA can modulate key immune-related pathways and reverse pro-inflammatory gene expression changes induced by TWEAK and TNF-α in HaCaT cells.

3.3 GA Inhibits HaCaT and Macrophage Inflammation via NF-κB and MAPK Pathways

Studies have shown that TWEAK and TNF exert potent synergistic effects in upregulating multiple psoriasis-associated genes in human keratinocytes, including *IL23A*, *IL36G*, and various chemokines. Simultaneously, TWEAK enhances the production of the psoriasis- specific chemokine *CCL20*, further promoting skin inflammation[32].

Just Accepted



Just Accepted

Figure 1 GA inhibits the abnormal HaCaT cell proliferation induced by TNF-α or TNF-α Combined with TWEAK. (a) Cell viability of HaCaT cells treated with different concentrations of TNF-α. (b) Schematic diagram of TNF-α and GA stimulation of HaCaT cells. (c) Dose-dependent inhibitory effects of GA on the enhanced cell viability of HaCaT cells induced by 60 ng/mL TNF-α. (d) Representative fluorescence microscopy images showing the suppressive effect of GA on TNF-α-induced proliferation of HaCaT cells after indicated treatments. (e-f) Flow cytometry analysis of GA-mediated inhibition of TNF-α-induced HaCaT cell proliferation after indicated treatments. (g) Effects of TWEAK or TWEAK+TNF-α treatment on the proliferation and cell viability of HaCaT cells. (h) Schematic diagram of TWEAK, TNF-α and GA stimulation of HaCaT cells. (i) Dose-dependent inhibitory effects of GA on the enhanced cell viability of HaCaT cells induced by the co-stimulation of TWEAK and TNF-α. (j) Representative fluorescence microscopy images showing

the inhibitory effect of GA on TWEAK- and TNF-α-induced HaCaT cell proliferation. (k-l) Flow cytometry analysis of GA-inhibited proliferation in HaCaT cells induced by TWEAK and TNF-α. All statistical data are presented as mean ± SD, $n = 3$. *$p < 0.05$, **$p < 0.01$, ***$p < 0.001$. Scale bar =100 μm.

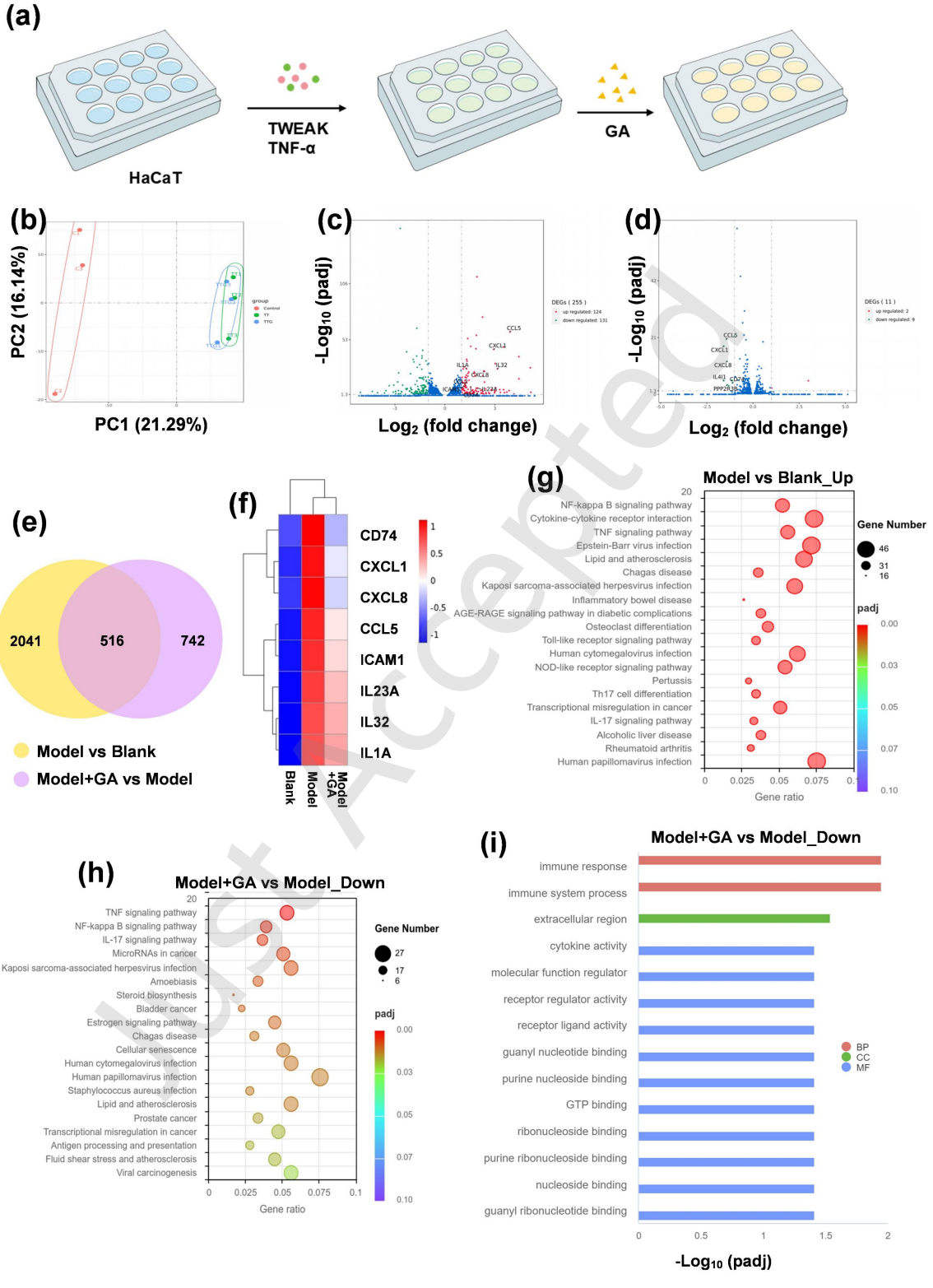


Figure 2 GA inhibits TWEAK/TNF-α-induced inflammatory signaling in HaCaT cells. (a) Schematic diagram of sample preparation process (b) Principal component analysis (PCA) of the replicate samples. (c, d) Volcano plots of differentially expressed genes (DEGs) in comparisons between the Blank, Model, and Treatment groups. (e) Venn diagram of DEGs unique and common to the different group comparisons. (f) Heatmap of DEGs showing hierarchical clustering across sample groups. (g, h) KEGG pathway enrichment analysis of selected DEGs. (i) GO enrichment analysis of DEGs between the Model and Treatment groups.

Just Accepted

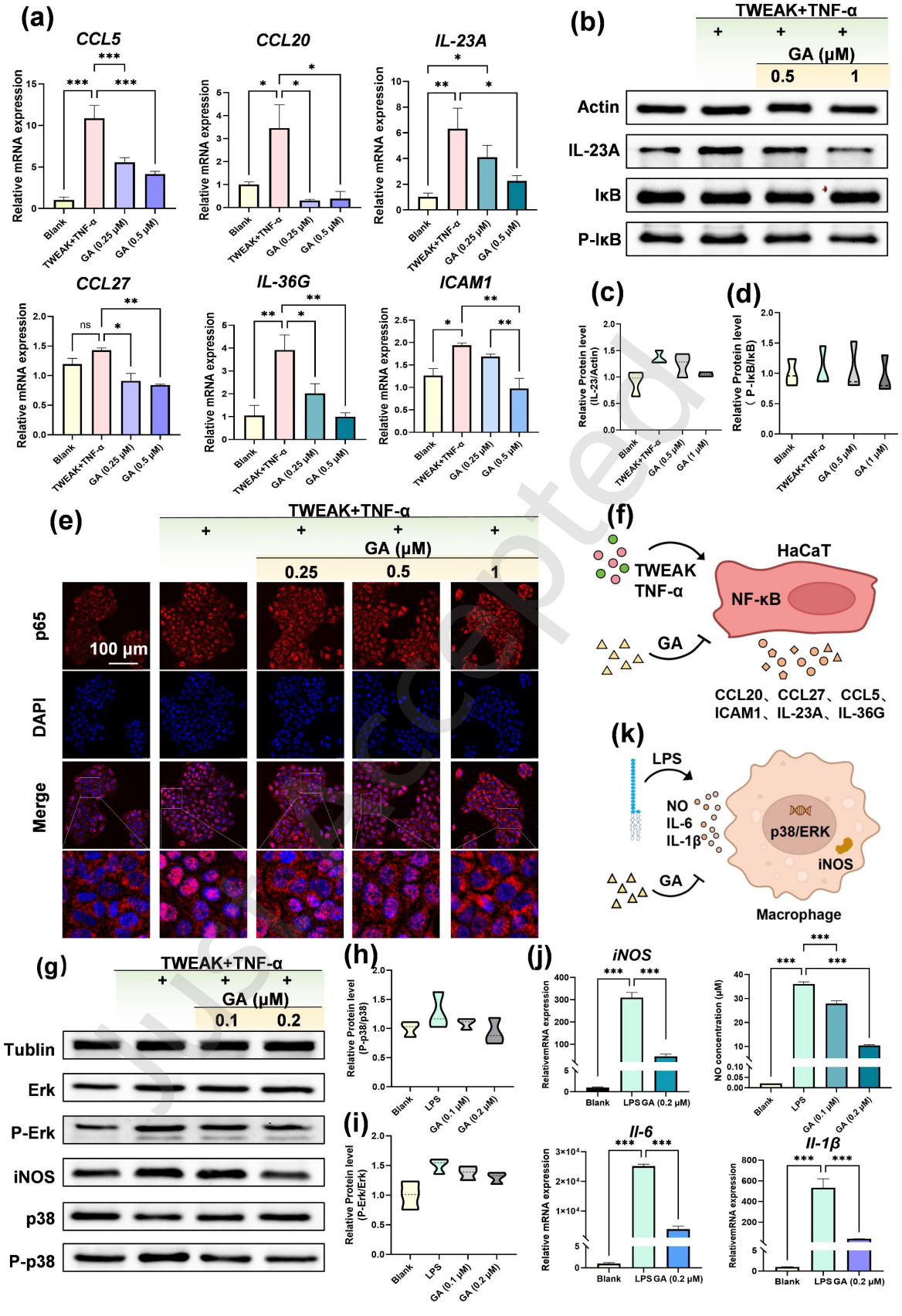


Figure 3 GA inhibits TWEAK and TNF-α-induced inflammation in HaCaT cells and LPS-induced inflammation in RAW264.7 cells. (a) Relative mRNA expression levels of inflammatory mediators (CCL5, CCL20, CCL27, ICAM1, IL-36G, and IL-23A) in HaCaT cells after indicated treatments. (b-d) Western blot analysis showing protein expression levels of IL-23, p-IκB, and IκB in HaCaT cells after indicated treatments (b), with quantitative analysis shown in (c) and (d). (e) Representative fluorescence micrographs of NF-κB p65 nuclear translocation after indicated treatments. (f) Proposed anti-inflammatory mechanism of GA in keratinocytes. (g-i) Western blot analysis and quantification of relevant proteins in RAW264.7 cells after indicated treatments. (j) Relative mRNA expression of iNOS, Il-6, and Il-1β, and supernatant concentration of NO in RAW264.7 cells after indicated

treatments. (k) Proposed anti-inflammatory mechanism of GA in macrophages. All statistical data are presented as mean ± SD, $n = 3$. *$p < 0.05$, **$p < 0.01$, ***$p < 0.001$. Scale bar, 100 μm.

CCL27 is a skin- specific chemokine expressed by cutaneous epithelial cells, and its receptor *CCR10* is expressed by skin lymphocytes. The CCL27/CCR10 axis has long been considered to contribute to inflammatory skin diseases, including psoriasis, by facilitating the migration of pathogenic T cells into the skin[33]. To further validate the above transcriptomic experimental results, we conducted the following experiments. Q-PCR analysis indicated that GA could significantly inhibit the upregulation of *CCL5*, *ICAM1*, *IL-23A*, and other related gene expressions induced by TWEAK and TNF-α in HaCaT cells (Fig. 3(a)). Results from Western blot demonstrated that GA attenuated the P-IκB to IκB ratio, which inhibits NF-κB activity by retaining more IκB to sequester NF-κB in an inactive state, and downregulating IL-23A, a critical driver of psoriasis pathogenesis, as an outcome of suppressed NF-κB signaling (Fig. 3(b)-(d)). TWEAK combined with TNF-α could induce p65 nuclear translocation (a key event and hallmark of NF-κB activation) in HaCaT cells (Fig. S4, 5), while this process was inhibited when GA was applied (Fig. 3(e)).
Collectively, GA inhibits NF-κB activation and reduces the expression of downstream inflammatory factors stimulated by TWEAK and TNF-α (Fig. 3(f)). Meanwhile, IL-17 plays a pivotal role in psoriasis pathogenesis by driving epidermal hyperplasia and sustaining chronic inflammation[34]. We confirmed that IL-17A, when combined with the two aforementioned cytokines, can promote p65 nuclear translocation as well (Fig. S6), while GA can reduce the elevated expression of inflammatory mediators induced by these three cytokines (Fig. S7). In conclusion, GA can inhibit NF-κB activation and the secretion of proinflammatory cytokines, thus holding potential therapeutic implications for psoriasis.

As demonstrated in numerous studies, macrophages play a pivotal role in psoriasis pathogenesis[35]. They release proinflammatory signaling molecules such as NO, IL-6, and IL-1β, which contribute to epidermal inflammation[36]. Activation of MAPK in macrophages leads to the secretion of inflammatory cytokines[37-39]. In our study, Western Blot analysis indicated that in LPS-stimulated RAW264.7 cells, the MAPK pathway-related proteins p-p38, p-Erk, and iNOS were significantly upregulated. However, following GA treatment, the protein levels of p-p38 and p-Erk decreased (Fig. 3(g)-(i)). Meanwhile, GA treatment significantly reduced the relative expression levels of *Il-1β*, *Il-6*, and *iNOS* genes and inhibited NO production in RAW264.7 cells (Fig. 3(j)). These results suggest that GA may exert a beneficial effect on psoriasis by modulating macrophage-related inflammatory responses (Fig. 3(k)). Collectively, the results indicate that GA is a promising small molecule for psoriasis treatment through its anti-inflammatory effects, although an appropriate delivery method remains to be developed.

3.4 Preparation and characterization of PVA/HA air-bubble MNs and GA NPs

While GA showed tremendous potential for treating psoriasis, it is still challenge to obtain efficient transdermal delivery. Air-bubble microneedles represent a promising platform for transdermal drug delivery, owing to their unique structure that enables rapid detachment from the backing layer and subsequent drug release[30, 40]. As suggested by previous studies, the presence of HA facilitates air gap formation[30]. Therefore, we utilized a composite of PVA and HA for microneedle fabrication, aiming to produce bubble microneedles while allowing the dissolution time of the needle tips to be tunable by incorporating PVA. Both of PVA and HA provides robust mechanical strength, excellent biocompatibility and biodegradability[41, 42]. In this study we fabricated the PVA/HA microneedles through five consecutive steps (Fig. 4(a)). In this process, air became trapped at the interface between the two layers when the backing solution is added after the tip solution is scraped off, and is subsequently preserved upon drying. Interestingly, we found that the air-gap volume could be readily tuned by varying the PVA-to-HA mass ratio (Fig. 4(b)).

In previous studies, air bubble formation has been attributed to the backing solution and the vacuum application time[30, 40]. Then, we first hypothesized that the viscosity of the microneedle solutions may affect bubble formation. However, although increasing the PVA content in the PVA/HA blends elevated viscosity and reduced the air gap size, pure PVA, which had the lowest viscosity, conversely showed no air gap formation at the microneedle tips (Fig. S8). Furthermore, we evaluated the impact of vacuum application time on air gap size. The results showed that the vacuum duration indeed led to a minor reduction in air gap dimensions (Fig. S9). However, since the vacuum application time was kept constant across all formulations in our experiments, it was not a primary factor affecting bubble size in this study.

Both HA and PVA form films after drying[43, 44], we therefore reasonably speculate that the thickness of the dried films formed by different materials may affect bubble size. Our experiments showed that under identical volumes, pure PVA formed relatively thick films on drying (~115.49 μm), whereas the HA system formed significantly thinner films (~66.29 μm). In PVA/HA blends, the film thickness increased progressively with higher PVA content (Fig. 4(c) and S10). This suggests that air gap formation is more closely related to the film thickness of dried HA and PVA. The air-gap size is thus primarily determined by the thickness of the dried films, which varies with the PVA-to-HA ratio. Mechanistically, air is trapped in the depression formed during the drying step, and the solution network stabilizes the structure in the drying process[45, 46].

Additionally, mechanical testing revealed that the stiffness of the microneedle tips varied significantly with the polymer ratio: pure PVA MNs exhibited the weakest mechanical strength, whereas pure HA MNs were the strongest (Fig. 4(d)).

Under Review

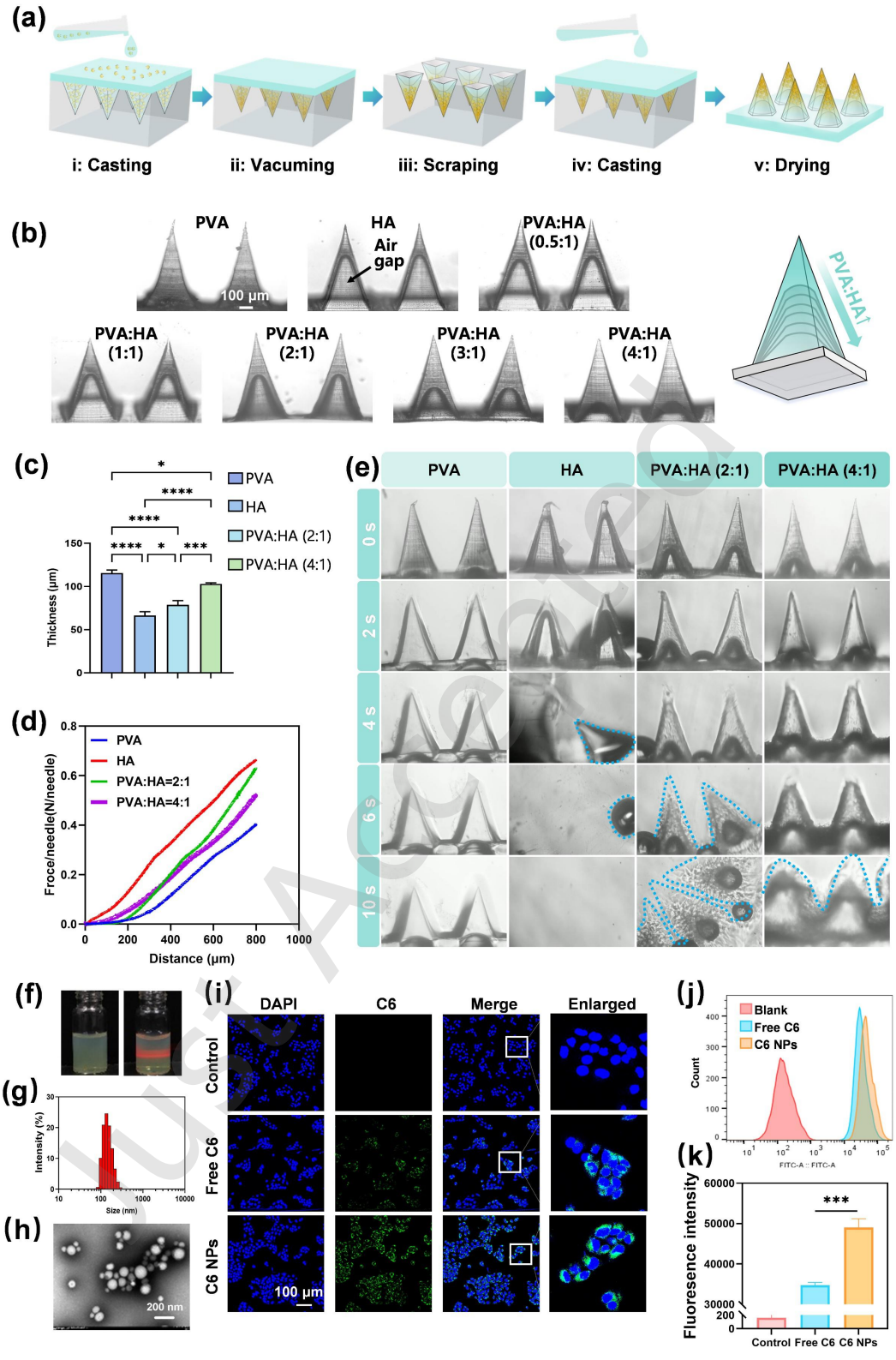


Figure 4 Preparation and characterization of PVA/HA air-bubble MNs and GA NPs. (a) Schematic illustration of the fabrication process of air-bubble MNs. (b) Optical images of MNs prepared with PVA, HA alone or with different PVA: HA ratios. Scale bar = 100 μm. (c) Thickness of dried films derived from equal-volume PVA, HA, and PVA/HA solutions at different ratios. (d) Mechanical strength test results of different MN patches. (e) Dissolution behavior of different microneedles in PBS over time. (f) Appearance of GA NPs. (g) Size distribution of GA NPs. (h) TEM images of GA NPs. (i) Fluorescence microscopy images of the cellular uptake of free C6 and C6-labelled GA NPs. Scale bar, 100 μm. (j) Flow cytometry analysis of cellular uptake of GA NPs. (k) Quantitative analysis of cellular fluorescence intensity of GA NPs. All statistical data are presented as mean ± SD, $n = 3$. ***$p <$ 0.001.

In vitro dissolution assays in PBS further demonstrated that HA MN tips dissolved almost instantly, whereas pure

PVA MNs exhibited the slowest dissolution rate. In the composite systems, the dissolution rate decreased proportionally as the PVA content increased (Fig. 4(e)). However, excessive dissolution rates is not necessarily desirable, as it may lead to premature burst release before the MNs have adequately penetrated the skin, thereby compromising the overall delivery efficiency. Meanwhile, overly large air gaps may compromise the drug-loading capacity of the MNs. Therefore, we optimally selected a PVA-to-HA ratio of 4:1 for subsequent MN fabrication, balancing mechanical strength, dissolution kinetics, and air gap volume.

Then, to achieve site-specific loading of GA at the microneedle tips, we encapsulated GA into PLGA nanoparticles, an FDA-approved pharmaceutical excipient. The resulting GA NPs exhibited a hydrodynamic particle size of 141.81 ± 6.5 nm, with a polydispersity index of 0.29 ± 0.06 and a zeta potential of -6.35 ± 0.46 mV. The encapsulation efficiency and drug loading capacity were 79.65 ± 0.44% and 19.91 ± 0.11%, respectively (Fig. 4(f)-(h) and Table S1). Because nanomedicines typically exhibit enhanced cellular internalization compared to free drugs[10], we evaluated their cellular uptake in HaCaT cells. Consistent with previous reports, the uptake of C6-NPs was significantly higher than that of free C6 in HaCaT cells, indicating that he nano-formulation substantially facilitated the cellular uptake of GA (Fig. 4(i)-(k)), which represents one of the key advantages of nanomedicines.

3.5 Characterization and Transdermal Delivery Performance of GA NP-Loaded Air-Bubble Microneedles

The casting solution demonstrated shear-thinning behavior (Fig. S11), which facilitated the GA NPs deposit at the needle tip. The deposition primarily occurred within a range of approximately 250 μm from the tip in PVA/HA-made microneedles (Fig. 5(a), (b)). The microneedles are arranged in a 12 × 12 array, with pyramid-shaped structures. Each needle has a height of approximately 750 μm, and the base diameter of each is approximately 400 μm (Fig. 5(c)). To confirm whether the mechanical strength of the MNs was sufficient for skin insertion, the displacement–force curves were examined. The GA NP- loaded microneedles withstood a force of approximately 0.34 N per needle at a displacement of 0.4 mm, indicating sufficient strength to penetrate the skin (Fig. 5(d))[47-49]. The GA loading capacity of the microneedles was 16.98 ± 0.54 μg. When stored at room temperature for 1 month, the drug loading capacity remained unchanged, confirming the excellent stability of the encapsulated drug under standard storage conditions (Fig. 5(e)). In addition, we also compared the air gap size before and after drug loading, and the results revealed no significant difference, suggesting that the encapsulation of nanoparticles at the microneedle tips did not affect bubble formation (Fig. S12).

We tested drug release from the microneedle patch by placing it directly in PBS. Results showed 85.96 ± 0.22% cumulative release over 12 h (Fig. 5(f)). Furthermore, *ex vivo* transdermal delivery of GA NPs via the microneedle patch reached 94.66 ± 3.08%. In stark contrast, topical application of the GA NPs suspension alone (without microneedle assistance) resulted in a mere 5 ± 0.28% permeation. This confirms that the microneedle patch delivery method markedly boosts transdermal drug release efficiency (Fig. 5(g), (h)). The difference may be related to differences in the experimental configuration, sampling duration, and drug partitioning between the skin tissue and receptor compartment.

Laser confocal microscopy was employed for 3D reconstruction of the patch before and after application to pig skin. Results confirmed successful skin penetration and dissolution of our microneedle, with a drug penetration depth of approximately 240 μm, which generally matches the height of the precipitated GA NPs (Fig. 5(i), (j)). To assess the skin recovery after microneedle has been applied, it was pressed onto mouse skin for a set time then removed. Immediately after, clear pores were visible; these gradually faded and nearly fully healed by 90 min. No redness or swelling occurred during application (Fig. S13). In addition, the microneedle patches were stored at room temperature for 4 days. The results showed that the patches exhibited a certain degree of hygroscopicity, highlighting the necessity of storing them in a desiccator to avoid compromising their penetration performance during use (Fig. S14).

3.6 GA NP-loaded Microneedles Alleviate IMQ-Induced Psoriasis-like skin Inflammation in Mice

To evaluate the therapeutic efficacy of our microneedle patches for psoriasis, we utilized an imiquimod (IMQ)-induced psoriasis-like mouse model (Fig. 6(a)). While it does not recapitulate the chronic relapsing nature of human psoriasis, this well-accepted model is suitable to explore IL-23/IL-17-mediated psoriasiform skin inflammation and assess the efficacy of our microneedle therapy. Mice were randomly allocated into seven groups: Normal, Model, Blank MNs, MNs-NPs, MNs-GA NPs (1 mg/kg, low dose of GA, LD MNs-GA NPs), MNs-GA NPs (2 mg/kg, high dose of GA, HD MNs-GA NPs), dexamethasone (Dex)-treated positive control group. The Psoriasis Area and Severity Index (PASI), which quantifies skin erythema, scaling, and thickness, serving as the key metric to assess lesion severity[50, 51]. As shown in Figure 6(b), (c) the Model Group gradually developed erythema, increased scaling (PASI scores progressively increased until day 6) with obvious infiltrative erythema, scaling, and stratum corneum thickening. The HD MNs-GA NPs group yielded PASI scores comparable to those of the Dex group, while the LD MNs-GA NPs groups resulted in only modest skin lesion improvement. Starting from day 3, IMQ-modeled mice exhibited significant weight loss, indicating IMQ's impact on mouse weight. Notably, the HD MNs-GA NPs group exhibited a more stable body weight trajectory in mice following treatment compared to the other groups, whereas mice treated with Dex showed a tendency towards weight loss (Fig. 6(d)). The levels of hematological parameters (white blood cells, monocytes, neutrophils) and serum biochemical parameters (ALT, AST, CREA, UREA) showed no significant differences between the blank/drug-loaded microneedle groups and the normal control group, indicating that the blank and drug-loaded microneedles do not cause systemic

Just Accepted

toxicity or impair liver/kidney function in treated mice (Fig. 6(e)-(k)).

Having analyzed the general phenotypic data, we now delve into the histological and molecular-level insights, which allow for a more mechanistic understanding of the observed outcomes. Compared with the normal mice, the model group exhibited marked hyperplasia of the epidermal spinous layer. The stratum corneum was significantly thickened, and crust formation was visible, collectively indicating successful modeling. In the Blank MNs group and the MNs-NPs group, there was no notable inhibition of the excessive stratum corneum thickening. Conversely, the LD MNs-GA NPs group, HD MNs-GA NPs group, and Dex group effectively inhibited the excessive thickening of the stratum corneum (Fig. 7(a), (b)). Ki67 staining indicated that the model group exhibited a marked increase in proliferating cells. In contrast, the LD MNs-GA NPs group showed a slight reduction in cell proliferation, while the HD MNs-GA NPs group and the Dex group demonstrated a significant decrease in stratum corneum cell proliferation (Fig. 7(c), (d)). *Il-23/Il-17* plays an important role in the pathogenesis of psoriasis-like skin inflammation on the inflammatory axis, and its role has been confirmed in many studies. *Il-23* and *Il-17* are commonly considered the primary therapeutic targets in psoriasis[52]. Immunofluorescence staining of the lesion area revealed that, relative to the model group, the LD MNs-GA NPs group, HD MNs-GA NPs group, and Dex group exhibited notable reductions in *Il-17* and *Il-23* expression levels (Fig. 7(e)-(h)). Given that HD MNs-GA NPs exhibited superior therapeutic efficacy compared to LD MNs-GA NPs, we subsequently focused on analyzing the HD MNs-GA NPs-treated group. Q-PCR analysis was then performed. When compared with the model group, the HD MNs-GA NPs group exhibited a significant reduction in the relative mRNA expression levels of *Il-17* and *Il-23*. Concomitantly, *Ccl5* and *Ccl20* are pivotal in recruiting inflammatory cells and amplifying the local inflammatory response. Their relative mRNA expression levels were also notably decreased in this group owing to the regulatory effect of GA (Fig. 7(i)-(l)). The above histological data indicate that MNs-GA NPs reduce epidermal thickening and abnormal keratinocyte proliferation in psoriatic skin, as well as decrease the secretion of psoriasis-associated cytokines and chemokines.

Psoriasis patients present with distinct scaly red plaques. Histologically, epidermal hyperplasia is observed, accompanied by prominent infiltration of inflammatory cells such as lymphocytes, neutrophils, and macrophages[53]. Macrophage polarization exhibits great heterogeneity and is involved in tissue remodeling and pathogenesis[54]. Compared with the normal group, the model group showed a significant increase in M1-type macrophages. Compared with the model group (3.15%), the HD MNs-GA NPs (1.71%) and the Dex group (1.81%) both showed a decrease in M1-type macrophages (Fig. 8(a), (e)). M2-type macrophages were significantly elevated in the HD MNs-GA NPs group (4.58%) compared to other groups (Fig. 8(b), (f)). Studies have reported that γδ-low T cells are the primary source of IL-17A production[55]. As depicted in Figure 8(c), (d) and (g), (h), the model group (16.1% and 18.8%) exhibited a significant elevation in neutrophils and IL-17$^+$ γδ-low T cells, whereas these levels were markedly reduced in the HD MNs-GA NPs (10.8% and 7.58%) and Dex groups (10.3% and 9.18%). The above experimental results indicate that HD MNs-GA NPs treatment can inhibit the excessive proliferation of keratinocytes and related inflammatory responses in the psoriatic lesion areas of mice induced by IMQ.

Just Accepted

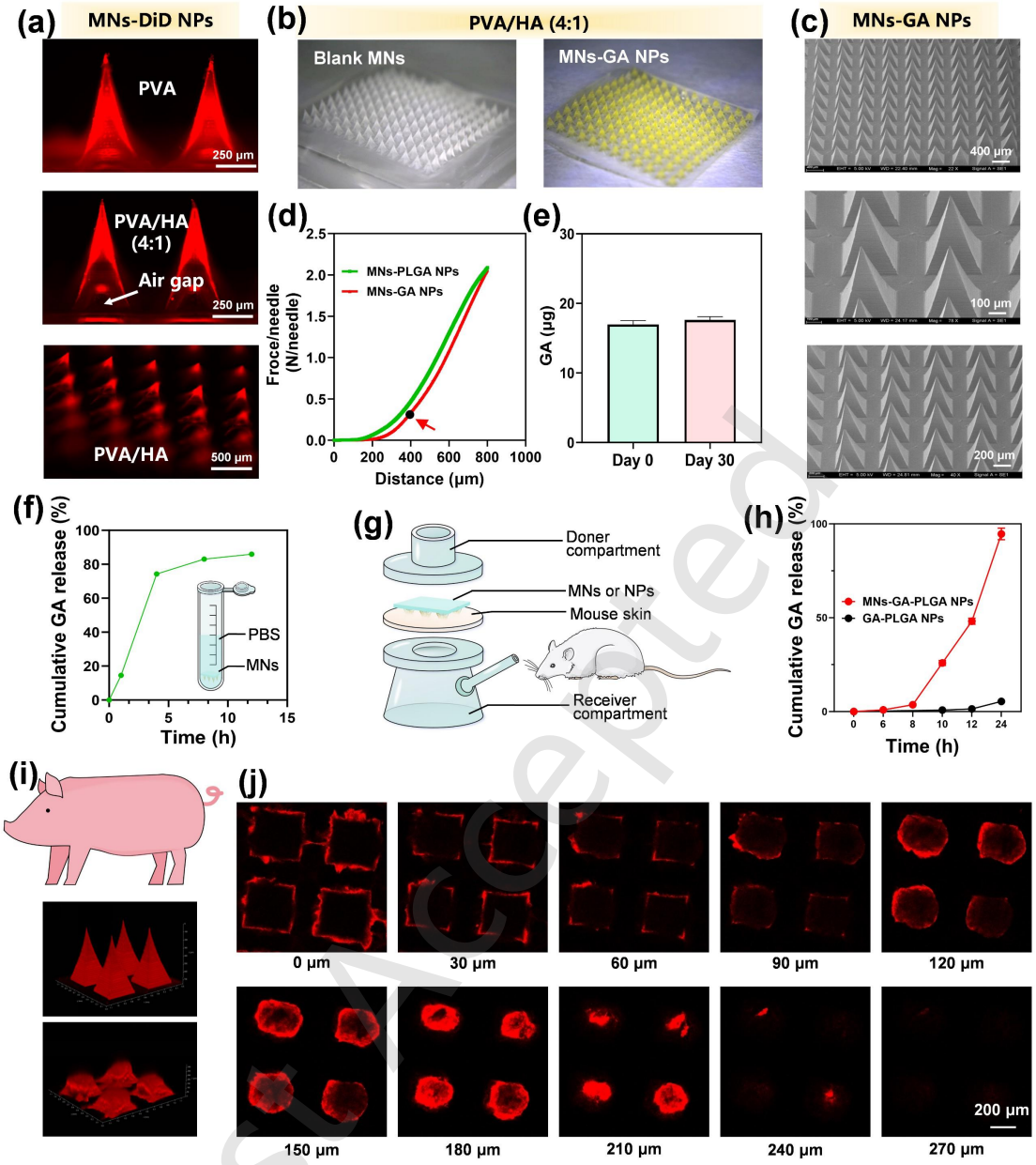


Figure 5 Characterization of PVA/HA air-bubble MNs. (a) Fluorescence images of MNs fabricated using PVA alone versus the PVA/HA composite. Scale bars, 250 (upper and middle) and 500 (lower) μm. (b) Representative appearance images comparing blank MNs and GA NP-loaded MNs. (c) SEM images of GA NP-loaded PVA/HA MNs at various magnifications. (d) Mechanical strength profiles of PLGA NP-loaded and GA NP-loaded MN patches. (e) Drug loading capacity of GA NP-loaded MN patches before and after one month of storage. (f) *In vitro* cumulative release kinetics of GA from the MN patches in PBS. (g-h) *Ex vivo* transdermal permeation kinetics of GA NPs delivered via MN patches versus topical suspension over 24 h. (i) Reconstructed 3D confocal images of microneedles before and after dissolution in porcine skin. (j) Fluorescence images indicating the penetration depth of the drug within the skin. Scale bar, 200 μm.

Just Accepted

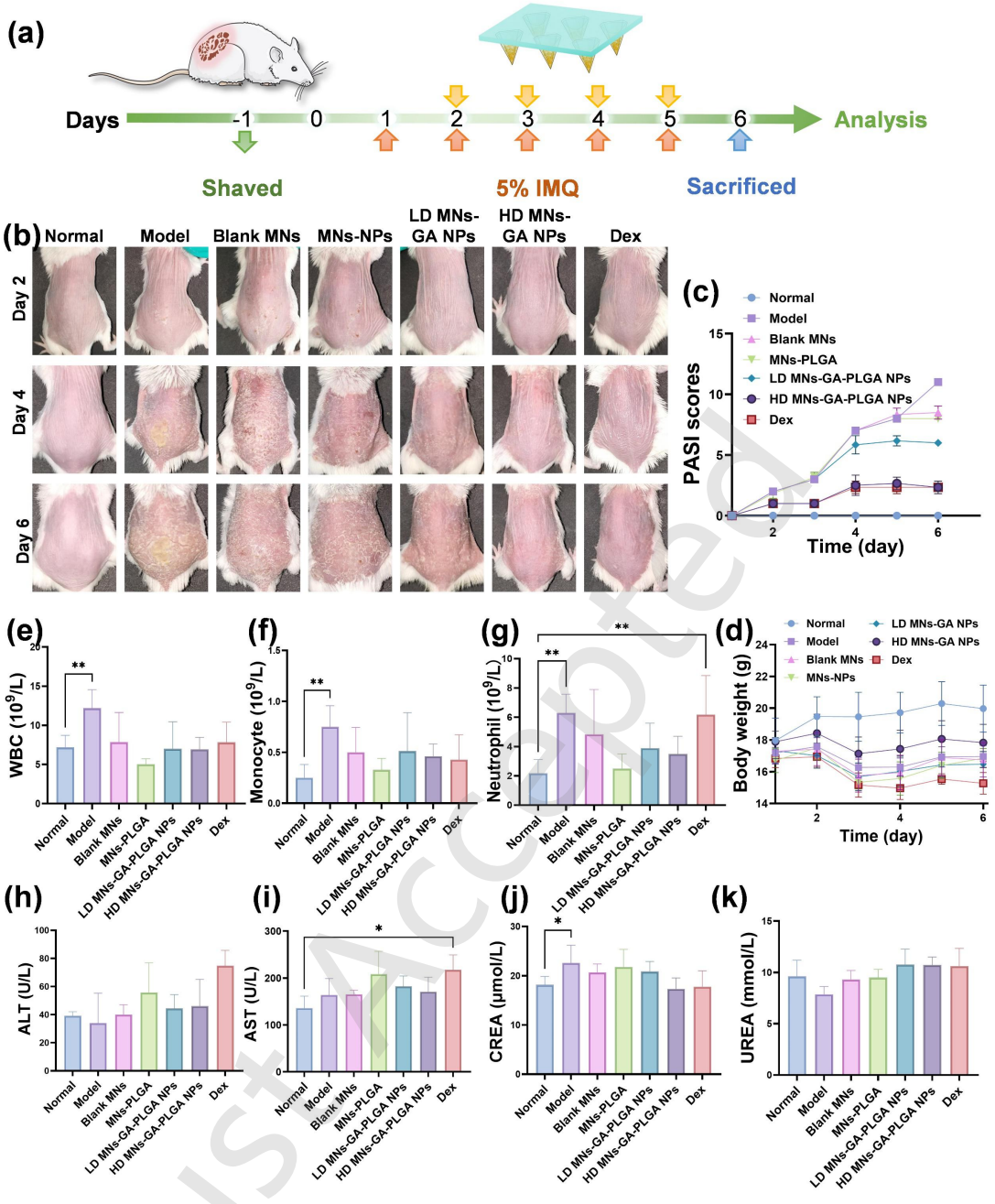


Figure 6 Evaluation of the *in vivo* therapeutic efficacy of GA NP-loaded microneedle patches for psoriasis treatment. (a) Schematic of the experimental timeline for treating IMQ-induced psoriasis-like mouse models using MN patches. (b) Representative photographs of psoriatic lesions on mouse backs across different treatment groups including Normal control, Model, Blank MNs, MNs-GA NPs, LD MNs-GA NPs (low dose of GA), HD MNs-GA NPs (high dose of GA), Dex. (c) PASI scores of the lesion areas after indicated treatments. (d) Body weight changes of mice throughout the treatment period after indicated treatments. (e-g) Levels of white blood cells (WBC), monocytes, and neutrophils in peripheral blood from each group. (h-k) Serum biochemical parameters including alanine aminotransferase (ALT), aspartate aminotransferase (AST), creatinine (CREA), and urea (UREA). All statistical data are presented as mean ± SD, $n = 6$. *$p < 0.05$, **$p < 0.01$.

Just Accepted

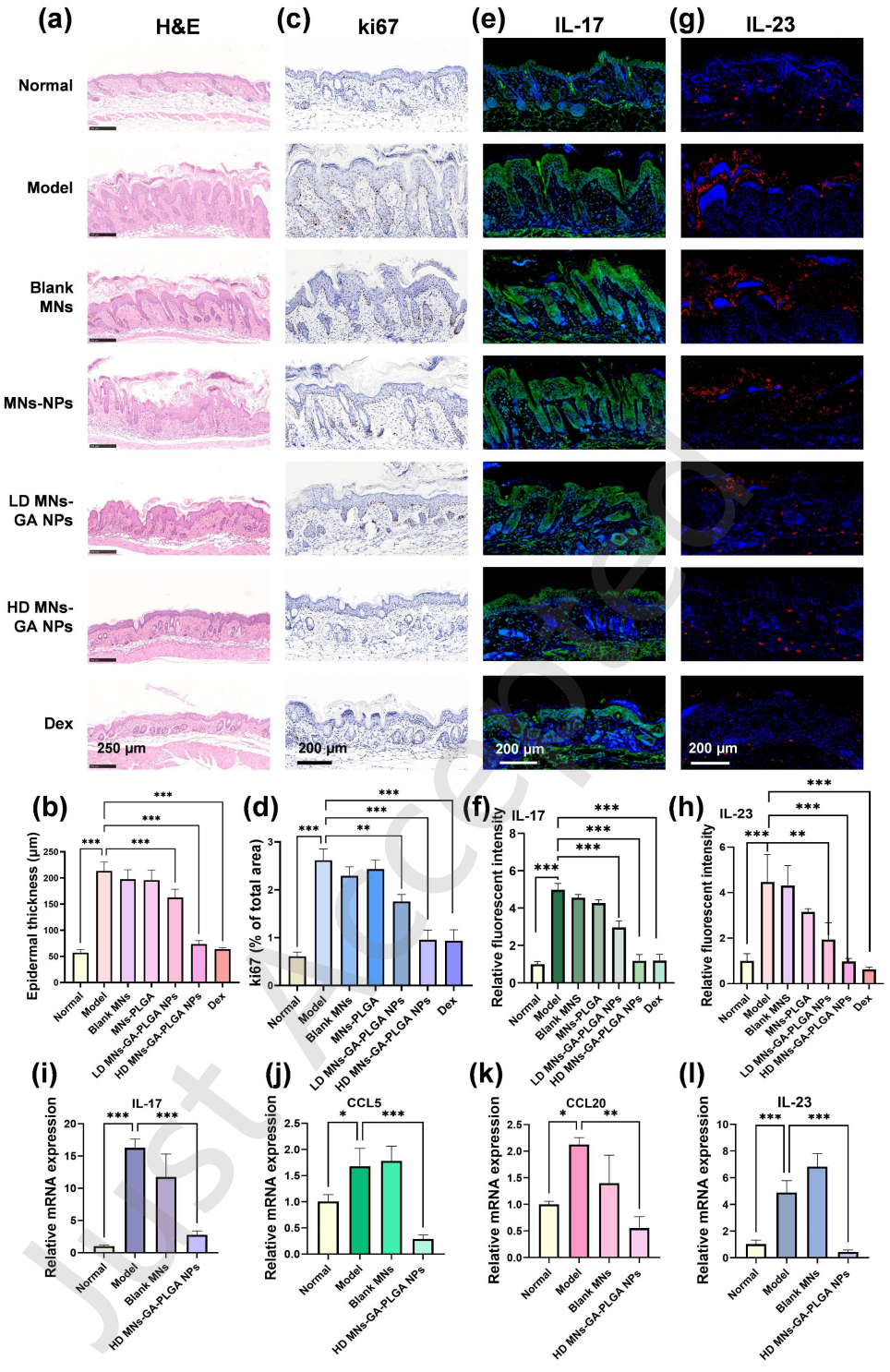


Figure 7 Mechanisms of GA NP-loaded microneedle patches for psoriasis treatment. (a) Representative H&E-stained skin sections from each experimental group. Scale bars, 250 μm. (b) Quantitative analysis of epidermal thickness based on H&E-stained sections after indicated treatments. (c) Representative immunohistochemical images of Ki67 staining after indicated treatments. Scale bar, 200 μm. (d) Quantitative analysis of Ki67-positive cells in different groups. (e, f) Representative IL-17 immunofluorescence staining images (e) and corresponding quantitative analysis of relative fluorescence intensity (f) in the psoriasis lesion area after indicated treatments. Scale bar, 200 μm. (g, h) Representative IL-23 immunofluorescence staining images (g) and corresponding quantitative analysis of relative fluorescence intensity (h) in the psoriasis lesion area after indicated treatments. Scale bar, 200 μm. (i-l) Relative mRNA expression levels of *Il-17* (i), *Ccl5* (j), *Ccl20* (k), and *Il-23* (l) in the skin lesions after indicated treatments. All statistical data are presented as mean ± SD, $n = 6$. *$p < 0.05$, **$p < 0.01$, ***$p < 0.001$.

Just Accepted

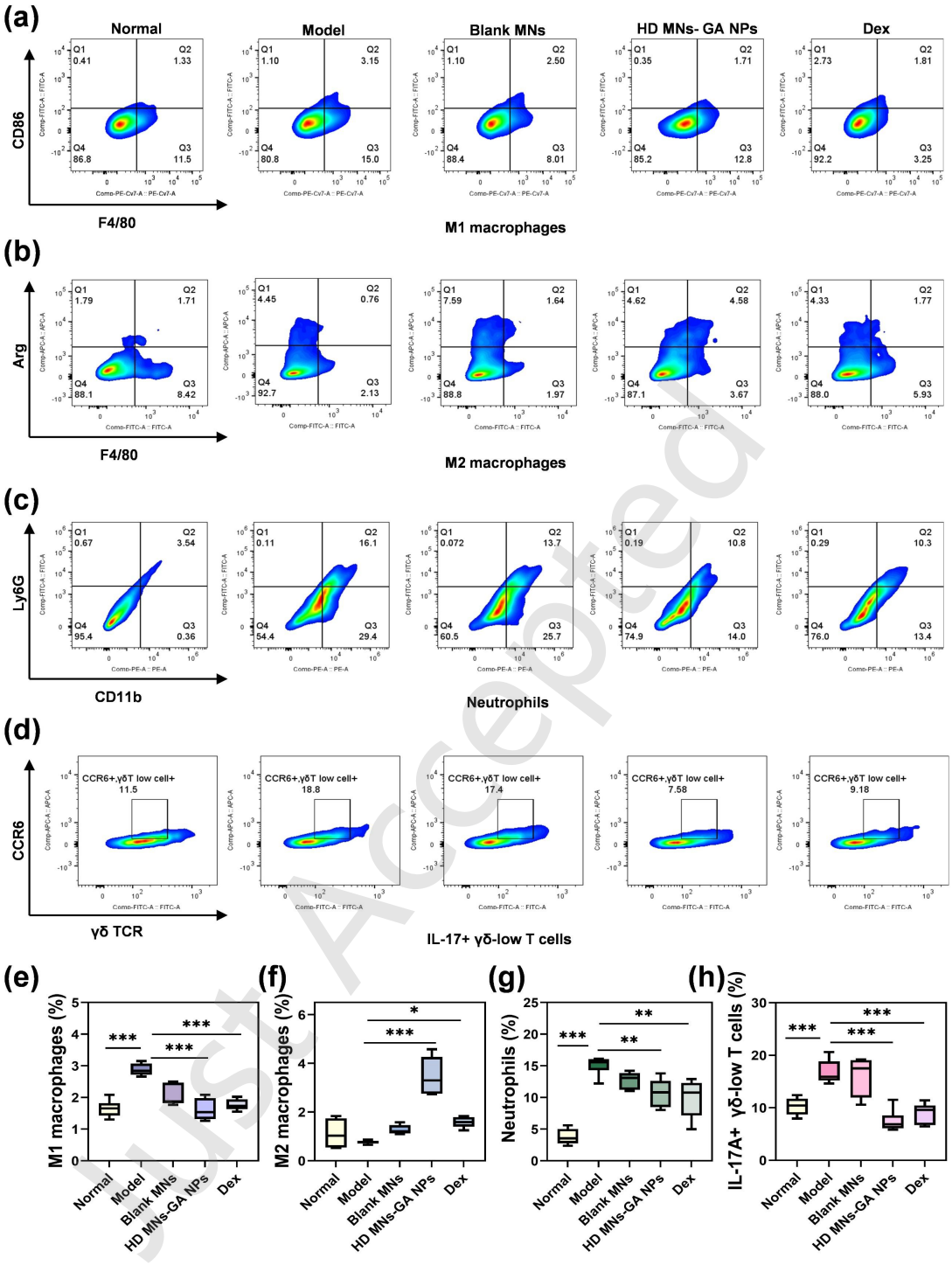


Figure 8 Immune modulation of the skin microenvironment by GA NP-loaded microneedle patches for psoriasis treatment. (a–d) Flow cytometry analysis of immune cell populations in psoriatic lesion tissues after indicated treatments: (a) M1 macrophages, (b) M2 macrophages, (c) neutrophils, and (d) IL-17$^+$ γδ-low T cells. (e) Quantitative analysis of the corresponding cell proportions after indicated treatments from (a-d). All statistical data are presented as mean ± SD, $n = 6$. $^{**}p < 0.01$, $^{***}p < 0.001$.

4. Conclusion

In this study, we investigated the therapeutic potential of Gambogic acid (GA), a natural compound whose application in psoriasis has received limited attention despite its great potential. To improve GA's transdermal permeability, we developed GA-loaded PLGA nanoparticles embedded in PVA/HA air-bubble microneedles. The bubble size was readily tunable simply by varying the PVA-to-HA ratio, which in turn affords tunable dissolution times of the microneedle system. We further investigated the underlying mechanism of air-bubble formation during fabrication, revealing that bubbles are generated at the interface when the backing solution is added after the tip solution has been scraped off. The thickness of the dried polymer film serves as the primary determinant of the final bubble size, with greater

Just Accepted

film thickness yielding smaller bubbles. We demonstrated that GA exerts anti-psoriatic effects by suppressing HaCaT cells hyperproliferation and by inhibiting the NF-κB and MAPK signaling pathways in HaCaT cells and macrophages, respectively. In an IMQ-induced psoriasis-like mouse model, GA nanoparticle-loaded microneedles exerted significant therapeutic effects, by alleviating skin lesions, inhibiting epidermal hyperplasia, and remodeling the skin immune microenvironment. The microneedle system showed no observed systemic toxicity. Collectively, this work not only supplies a novel drug candidate for psoriasis management but also establishes a new strategy for microneedle-mediated transdermal delivery.

Electronic Supplementary Material: Supplementary material is available in the online version of this article at https://doi.org/10.26599/NR.2026.94909245.

Acknowledgements

This study was financially supported by the National Natural Science Foundation of China (82405161), Natural Science Foundation of Sichuan Province (No. 2026NSFSC0609), the Tianfu E'mei Project of Sichuan Province (No. 1644, No. 2273), the Joint Innovation Fund of Health Commission of Chengdu and Chengdu University of Traditional Chinese Medicine (WXLH202402016), and Xinglin Scholar Research Promotion Program of Chengdu University of Traditional Chinese Medicine (QJRC2024018).

Declaration of competing interest

The authors declare that they have no known competing financial interests or personal relationships that could have appeared to influence the work reported in this paper.

Author contribution statement

Huan Yang, Dandan Mi and Rujing Wang conducted the experiments, analyzed the experimental data, and drafted the initial manuscript. Lan Zou, Yuyu Wei, and Yan Tang assisted in performing partial experiments. Yan Li and Wenwei Zuo participated in the research investigations, provided suggestions on experimental design, and revised the manuscript. Rujing Wang, Sanjun Shi, and Mengnan Zhao provided financial support for the study. Mengnan Zhao provided experimental ideas, academic guidance, and revised the manuscript. All authors have read, revised, and approved the final version of the manuscript.

Ethics statement

This study was conducted in accordance with the ARRIVE (Animal Research: Reporting of *In Vivo* Experiments) guidelines.

This study was approved by the Ethics Committee of Chengdu University of Traditional Chinese Medicine.

References

[1] Griffiths, C. E. M.;Armstrong, A. W.;Gudjonsson, J. E.; Barker, J. N. W. N. Psoriasis. *The Lancet* **2021**, *397*, 1301-1315.

[2] Grän, F.;Kerstan, A.;Serfling, E.;Goebeler, M.; Muhammad, K. Current Developments in the Immunology of Psoriasis. *The Yale journal of biology and medicine* **2020**, *93*.

[3] Gupta, R. K.;Gracias, D. T.;Figueroa, D. S.;Miki, H.;Miller, J.;Fung, K.;Ay, F.;Burkly, L.; Croft, M. TWEAK functions with TNF and IL-17 on keratinocytes and is a potential target for psoriasis therapy. *Sci Immunol* **2021**, *6*, eabi8823.

[4] Schukur, L.;Geering, B.;Charpin-El Hamri, G.; Fussenegger, M. Implantable synthetic cytokine converter cells with AND-gate logic treat experimental psoriasis. *Sci Transl Med* **2015**, *7*, 318ra201.

[5] Zhang, Z.;Wei, X.;Huang, Q.;Shi, Z.;Chen, X.;Wu, J.;Wang, X.;Li, J.;Gou, L.; Yang, J. Discovery of STING antagonists targeting cGAS-STING pathway to alleviate IMQ-induced psoriasis-like dermatitis. *European Journal of Pharmaceutical Sciences* **2025**, *210*, 107091.

[6] Gunter, N. V.;Teh, S. S.;Lim, Y. M.; Mah, S. H. Natural Xanthones and Skin Inflammatory Diseases: Multitargeting Mechanisms of Action and Potential Application. *Front Pharmacol* **2020**, *11*, 594202.

[7] Mi, D.;Liu, T.;Zou, L.;Wei, Y.;Zeng, J.;Nie, C.;Zeng, Y.;Wang, R.;Zhao, M.; Shi, S. A dual-asymmetric hemostatic Janus hydrogel patch inhibits postoperative recurrence and metastasis of triple-negative breast cancer by suppressing COX-2/PGE2 axis. *Biomaterials* **2026**, *334*, 124298.

[8] Ren, J.;Li, L.;Wang, Y.;Zhai, J.;Chen, G.; Hu, K. Gambogic acid induces heme oxygenase-1 through Nrf2 signaling pathway and inhibits NF-κB and MAPK activation to reduce inflammation in LPS-activated RAW264.7 cells. *Biomed Pharmacother* **2019**, *109*, 555-562.

[9] Lyu, S.;Zhang, X.;Tu, Z.;Zhou, H.;Ke, X.; Qu, Y. GPR108 is required for gambogic acid inhibiting NF-κB signaling in cancer. *Pharmacol Res* **2022**, *182*, 106279.

[10] Mi, D.;Li, J.;Wang, R.;Li, Y.;Zou, L.;Sun, C.;Yan, S.;Yang, H.;Zhao, M.; Shi, S. Postsurgical wound management and prevention of triple-negative breast cancer recurrence with a pryoptosis-inducing, photopolymerizable hydrogel. *J Control Release* **2023**, *356*, 205-218.

[11] Li, J.;Mi, D.;Wang, R.;Li, Y.;Zhao, M.; Shi, S. A lava-inspired proteolytic enzyme therapy on cancer with a PEG-based hydrogel enhances tumor distribution and penetration of liposomes. *J Nanobiotechnology* **2024**, *22*, 216.

[12] Mi, L.;Xing, Z.;Zhang, Y.;He, T.;Su, A.;Wei, T.;Li, Z.; Wu, W. Unveiling Gambogenic Acid as a Promising Antitumor Compound: A Review. *Planta Medica* **2024**, *90*, 353-367.

[13] Wen, J.;Pei, H.;Wang, X.;Xie, C.;Li, S.;Huang, L.;Qiu, N.;Wang, W.;Cheng, X.; Chen, L. Gambogic acid exhibits anti-psoriatic efficacy through inhibition of angiogenesis and inflammation. *J Dermatol Sci* **2014**, *74*, 242-250.

[14] Chowdhury, M. R.;Moshikur, R. M.;Wakabayashi, R.;Moniruzzaman, M.; Goto, M. Biocompatible ionic liquids assisted transdermal co-delivery of antigenic protein and adjuvant for cancer immunotherapy. *Int J Pharm* **2021**, *601*, 120582.

[15] Li, D.;Hu, D.;Xu, H.;Patra, H. K.;Liu, X.;Zhou, Z.;Tang, J.;Slater, N.; Shen, Y. Progress and perspective of microneedle system for anti-cancer drug delivery. *Biomaterials* **2021**, *264*, 120410.

[16] Banik, K.;Harsha, C.;Bordoloi, D.;Lalduhsaki Sailo, B.;Sethi, G.;Leong, H. C.;Arfuso, F.;Mishra, S.;Wang, L.;Kumar, A. P.; Kunnumakkara, A. B. Therapeutic potential of gambogic acid, a caged xanthone, to target cancer. *Cancer Lett* **2018**, *416*, 75-86.

[17] Sun, J.;Yang, Y.;Zheng, J.;Liang, H.;Yan, F.;Zhang, W.; Xie, W. Enhanced transdermal delivery of lidocaine cream via ultrasound and microneedle rollers. *Frontiers in Bioengineering and Biotechnology* **2025**, *13*.

[18] Xiang, W.;Jiang, X.; Guo, L. A Bibliometric Analysis of Microneedle-Mediated Drug Delivery: Trends, Hotspots, and Future Directions. *Drug Design, Development and Therapy* **2025**, *Volume 19*, 3805-3825.

[19] Tang, Y.;Liu, T.;Wang, C.;Xu, J.;Zhong, G.;Jing, Q.;Liu, J.;Gao, F.;Wang, R.;Zhao, M.; Shi, S. Janus microneedles enabling orderly vitiligo treatment through spatiotemporal sequential promoting melanogenesis to transfer via PAR2 activation. *Asian Journal of Pharmaceutical Sciences* **2026**, *21*.

[20] He, P.;He, C.;Guo, R.;Ou, Y.;Chang, Y.;Xie, Z.;Tang, X.;Xu, Y.;Zhao, Y.;Wang, H.;Guo, Z.;Bai, S.;Chen, Z.;Fan, F.;Du, G.; Sun, X. Tough and waterproof microneedles overcome mucosal immunotolerance by modulating antigen release patterns. *Journal of Controlled Release* **2025**,

Just Accepted

382, 113740.

[21] Suo, Z.;Xu, Y.;Zhang, A.;Cao, Y.;Liu, J.;Wang, H.; Zhong, R. Application of platelet-rich plasma lysate combined with hyaluronic acid microneedles for the treatment of alopecia. *Drug Deliv Transl Res* **2025**, *15*, 3517-3527.

[22] Yang, G.;Chen, Q.;Wen, D.;Chen, Z.;Wang, J.;Chen, G.;Wang, Z.;Zhang, X.;Zhang, Y.;Hu, Q.;Zhang, L.; Gu, Z. A Therapeutic Microneedle Patch Made from Hair-Derived Keratin for Promoting Hair Regrowth. *ACS Nano* **2019**, *13*, 4354-4360.

[23] Kim, S.;Yang, H.;Eum, J.;Ma, Y.;Fakhraei Lahiji, S.; Jung, H. Implantable powder-carrying microneedles for transdermal delivery of high-dose insulin with enhanced activity. *Biomaterials* **2020**, *232*, 119733.

[24] Kim, N. W.;Kim, S. Y.;Lee, J. E.;Yin, Y.;Lee, J. H.;Lim, S. Y.;Kim, E. S.;Duong, H. T. T.;Kim, H. K.;Kim, S.;Kim, J. E.;Lee, D. S.;Kim, J.;Lee, M. S.;Lim, Y. T.; Jeong, J. H. Enhanced Cancer Vaccination by In Situ Nanomicelle-Generating Dissolving Microneedles. *ACS Nano* **2018**, *12*, 9702-9713.

[25] Ruan, W.;Zhai, Y.;Yu, K.;Wu, C.; Xu, Y. Coated microneedles mediated intradermal delivery of octaarginine/BRAF siRNA nanocomplexes for anti-melanoma treatment. *Int J Pharm* **2018**, *553*, 298-309.

[26] Pan, J.;Ruan, W.;Qin, M.;Long, Y.;Wan, T.;Yu, K.;Zhai, Y.;Wu, C.; Xu, Y. Intradermal delivery of STAT3 siRNA to treat melanoma via dissolving microneedles. *Sci Rep* **2018**, *8*, 1117.

[27] Li, L.;Qin, W.;Ye, T.;Wang, C.;Qin, Z.;Ma, Y.;Mu, Z.;Jiao, K.;Tay, F. R.;Niu, W.; Niu, L. Bioactive Zn-V-Si-Ca Glass Nanoparticle Hydrogel Microneedles with Antimicrobial and Antioxidant Properties for Bone Regeneration in Diabetic Periodontitis. *ACS Nano* **2025**, 10.1021/acsnano.4c15227.

[28] Cheng, Y.;Zhang, X.;Wu, X.;Ding, Y.;Zhu, L.;Pan, J.;Zhao, Y.; Zhou, M. Multifunctional Microneedle Patches for Perivascular Gene Delivery and Treatment of Vascular Intimal Hyperplasia. *ACS Nano* **2024**, 10.1021/acsnano.4c09527.

[29] Yao, W. D.;Zhou, J. N.;Tang, C.;Zhang, J. L.;Chen, Z. Y.;Li, Y.;Gong, X. J.;Qu, M. Y.;Zeng, Q.;Jia, Y. L.;Wang, H. Y.;Fan, T.;Ren, J.;Guo, L. L.;Xi, J. F.;Pei, X. T.;Han, Y.; Yue, W. Hydrogel Microneedle Patches Loaded with Stem Cell Mitochondria-Enriched Microvesicles Boost the Chronic Wound Healing. *ACS Nano* **2024**, 10.1021/acsnano.4c06921.

[30] Yang, Y.;Chu, H.;Zhang, Y.;Xu, L.;Luo, R.;Zheng, H.;Yin, T.; Li, Z. Rapidly separable bubble microneedle patch for effective local anesthesia. *Nano Research* **2022**, *15*, 8336-8344.

[31] Greb, J. E.;Goldminz, A. M.;Elder, J. T.;Lebwohl, M. G.;Gladman, D. D.;Wu, J. J.;Mehta, N. N.;Finlay, A. Y.; Gottlieb, A. B. Psoriasis. *Nat Rev Dis Primers* **2016**, *2*, 16082.

[32] Sidler, D.;Wu, P.;Herro, R.;Claus, M.;Wolf, D.;Kawakami, Y.;Kawakami, T.;Burkly, L.; Croft, M. TWEAK mediates inflammation in experimental atopic dermatitis and psoriasis. *Nat Commun* **2017**, *8*, 15395.

[33] Li, C.;Xu, M.;Coyne, J.;Wang, W. B.;Davila, M. L.;Wang, Y.; Xiong, N. Psoriasis-associated impairment of CCL27/CCR10-derived regulation leads to IL-17A/IL-22-producing skin T-cell overactivation. *J Allergy Clin Immunol* **2021**, *147*, 759-763.e759.

[34] Lynde, C. W.;Poulin, Y.;Vender, R.;Bourcier, M.; Khalil, S. Interleukin 17A: toward a new understanding of psoriasis pathogenesis. *J Am Acad Dermatol* **2014**, *71*, 141-150.

[35] Zhu, Y.;Zhao, L.;Yan, W.;Ma, H.;Zhao, W.;Qu, J.;Zheng, W.;Zhang, C.;Du, H.;Yu, M.;Wan, N.;Ye, H.;Xie, Y.;Ke, B.;Xu, Q.;Sun, H.;Sun, Y.; Ouyang, Z. Celastrol directly targets LRP1 to inhibit fibroblast-macrophage crosstalk and ameliorates psoriasis progression. *Acta Pharmaceutica Sinica B* **2025**, *15*, 876-891.

[36] Sieminska, I.;Pieniawska, M.; Grzywa, T. M. The Immunology of Psoriasis-Current Concepts in Pathogenesis. *Clin Rev Allergy Immunol* **2024**, 10.1007/s12016-024-08991-7.

[37] Liu, J.;Tang, J.;Zuo, Y.;Yu, Y.;Luo, P.;Yao, X.;Dong, Y.;Wang, P.;Liu, L.; Zhou, H. Stauntoside B inhibits macrophage activation by inhibiting NF-κB and ERK MAPK signalling. *Pharmacol Res* **2016**, *111*, 303-315.

[38] Singh, V. K.;Sahoo, D.;Agrahari, K.;Khan, A.;Mukhopadhyay, P.;Chanda, D.; Yadav, N. P. Anti-inflammatory, anti-proliferative and anti-psoriatic potential of apigenin in RAW 264.7 cells, HaCaT cells and psoriasis like dermatitis in BALB/c mice. *Life Sci* **2023**, *328*, 121909.

[39] Thatikonda, S.;Pooladanda, V.;Sigalapalli, D. K.; Godugu, C. Piperlongumine regulates epigenetic modulation and alleviates psoriasis-like skin inflammation via inhibition of hyperproliferation and inflammation. *Cell Death Dis* **2020**, *11*, 21.

[40] Li, W.;Terry, R. N.;Tang, J.;Feng, M. R.;Schwendeman, S. P.; Prausnitz, M. R. Rapidly separable microneedle patch for the sustained release of a contraceptive. *Nat Biomed Eng* **2019**, *3*, 220-229.

[41] Jiang, X.;Zhang, W.;Terry, R.; Li, W. The progress of fabrication designs of polymeric microneedles and related biomedical applications. *BMEMat* **2023**, *1*, e12044.

[42] Wang, J.;Risola, D. D.;Mattioli, R.;Zoratto, N.;Mosca, L.;Meo, C. D.; Matricardi, P. Hyaluronan-Cholesterol nanogels embedding betamethasone for the treatment of skin inflammatory conditions. *International Journal of Pharmaceutics* **2025**, *668*, 124978.

[43] Alghasham, H. A. Development of wound healing scaffolds based on polymeric blends of polyvinyl alcohol and hyaluronic acid doped with super antibacterials of silver phosphate with magnesium vanadate. *New Journal of Chemistry* **2024**, *48*, 4529-4538.

[44] Li, Y.;Liu, X.;Lv, D.;Hou, S.;Yu, X.; Han, Y. Suppression of the Skin-Core Structure of Poly(vinyl alcohol) Films by Adding Urea/Diethanolamine to Improve the Mechanical and Optical Properties. *Macromolecules* **2024**, *57*, 6109-6122.

[45] Kudo, K.;Ishida, J.;Syuu, G.;Sekine, Y.; Ikeda-Fukazawa, T. Structural changes of water in poly(vinyl alcohol) hydrogel during dehydration. *J Chem Phys* **2014**, *140*, 044909.

[46] Holloway, J. L.;Lowman, A. M.; Palmese, G. R. The role of crystallization and phase separation in the formation of physically cross-linked PVA hydrogels. *Soft Matter* **2013**, *9*, 826-833.

[47] Wu, T.;Hou, X.;Li, J.;Ruan, H.;Pei, L.;Guo, T.;Wang, Z.;Ci, T.;Ruan, S.;He, Y.;He, Z.;Feng, N.; Zhang, Y. Microneedle-Mediated Biomimetic Cyclodextrin Metal Organic Frameworks for Active Targeting and Treatment of Hypertrophic Scars. *ACS Nano* **2021**, *15*, 20087-20104.

[48] Wang, H.;Wang, W.;Li, C.;Xu, A.;Qiu, B.;Li, F.; Ding, W. Flav7+DOX co-loaded separable microneedle for light-triggered chemo-thermal therapy of superficial tumors. *Chemical Engineering Journal* **2022**, *428*, 131913.

[49] Feng, Y.;Tang, Y.;Hu, J.;Chen, C.;Zhong, G.;Xiang, C.;Chen, N.;Bian, J.;Shi, S.; Zhang, Y. Phaseolus lunatus L. polysaccharide microneedles loaded with sinomenine hydrochloride for synergistic rheumatoid arthritis management and analgesia. *International Journal of Biological Macromolecules* **2025**, *306*, 141511.

[50] Zhu, J.;Yang, T.;Tang, M.;Yang, Z.;Pei, H.;Ye, H.;Tang, Y.;Cheng, Z.;Lin, P.; Chen, L. Studies on the anti-psoriasis effects and its mechanism of a dual JAK2/FLT3 inhibitor flonoltinib maleate. *Biomedicine & Pharmacotherapy* **2021**, *137*, 111373.

[51] Wang, Y.;Gao, J.;Yu, Y.;Zhou, L.;Wang, M.;Xue, W.;Liu, B.;Wu, X.;Wu, X.;Gao, H.;Shen, Y.; Xu, Q. A plant-derived glucocorticoid receptor modulator with potency to attenuate the side effects of glucocorticoid therapy. *British Journal of Pharmacology* **2023**, *180*, 194-213.

[52] Ghoreschi, K.;Balato, A.;Enerbäck, C.; Sabat, R. Therapeutics targeting the IL-23 and IL-17 pathway in psoriasis. *The Lancet* **2021**, *397*, 754-766.

[53] Hou, Y.;Zhu, L.;Tian, H.;Sun, H. X.;Wang, R.;Zhang, L.; Zhao, Y. IL-23-induced macrophage polarization and its pathological roles in mice with imiquimod-induced psoriasis. *Protein Cell* **2018**, *9*, 1027-1038.

[54] Yong, L.;Yu, Y.;Li, B.;Ge, H.;Zhen, Q.;Mao, Y.;Yu, Y.;Cao, L.;Zhang, R.;Li, Z.;Wang, Y.;Fan, W.;Zhang, C.;Wang, D.;Luo, S.;Bai, Y.;Chen, S.;Chen, W.;Liu, M.;Shen, J.; Sun, L. Calcium/calmodulin-dependent protein kinase IV promotes imiquimod-induced psoriatic inflammation via macrophages and keratinocytes in mice. *Nat Commun* **2022**, *13*, 4255.

[55] Lai, Y.;Wu, X.;Jiang, Z.;Fang, Y.;Liu, X.;Hong, D.;Jiang, Y.;Tan, G.;Tang, S.;Lu, S.;Wei, D.;Hwang, S. T.;Lam, K. S.;Wang, L.;Huang, Y.; Shi, Z. Topical treatment of tyrosine kinase 2 inhibitor through borneol-embedded hydrogel: Evaluation for preventive, therapeutic, and Recurrent management of psoriasis. *Bioact Mater* **2024**, *41*, 83-95.

Just Accepted

Electronic Supplementary Material

A tunable air-bubble microneedle system delivers gambogic acid for alleviating psoriasis-like skin inflammation

Huan Yang[1,§], Dandan Mi[1, §], Rujing Wang[2,§], Lan Zou[1], Yuyu Wei[1], Yan Tang[1], Yan Li[3], Wenwei Zuo[4], Sanjun Shi[1], and Mengnan Zhao [1]

[1] *Chinese Medicine Germplasm Resources Innovation and Effective Uses Key Laboratory of Sichuan Province, School of Pharmacy, School of Modern Chinese Medicine Industry, Chengdu University of Traditional Chinese Medicine, Chengdu, China*
[2] *School of Basic Medical Sciences, Chengdu University of Traditional Chinese Medicine, Chengdu, China*
[3] *Chengdu Brilliant Pharmaceutical Co., Ltd, Chengdu, China*
[4] *Department of General Surgery, Hospital of Chengdu University of Traditional Chinese Medicine, Chengdu, China*
[§] *Huan Yang, Dandan Mi, and Rujing Wang contributed equally to this work.*

Address correspondence to zhaomengnan@cdutcm.edu.cn

Supporting information to https://doi.org/10.26599/NR.2026.94909245

Just Accepted

Address correspondence to Mengnan Zhao, zhaomengnan@cdutcm.edu.cn

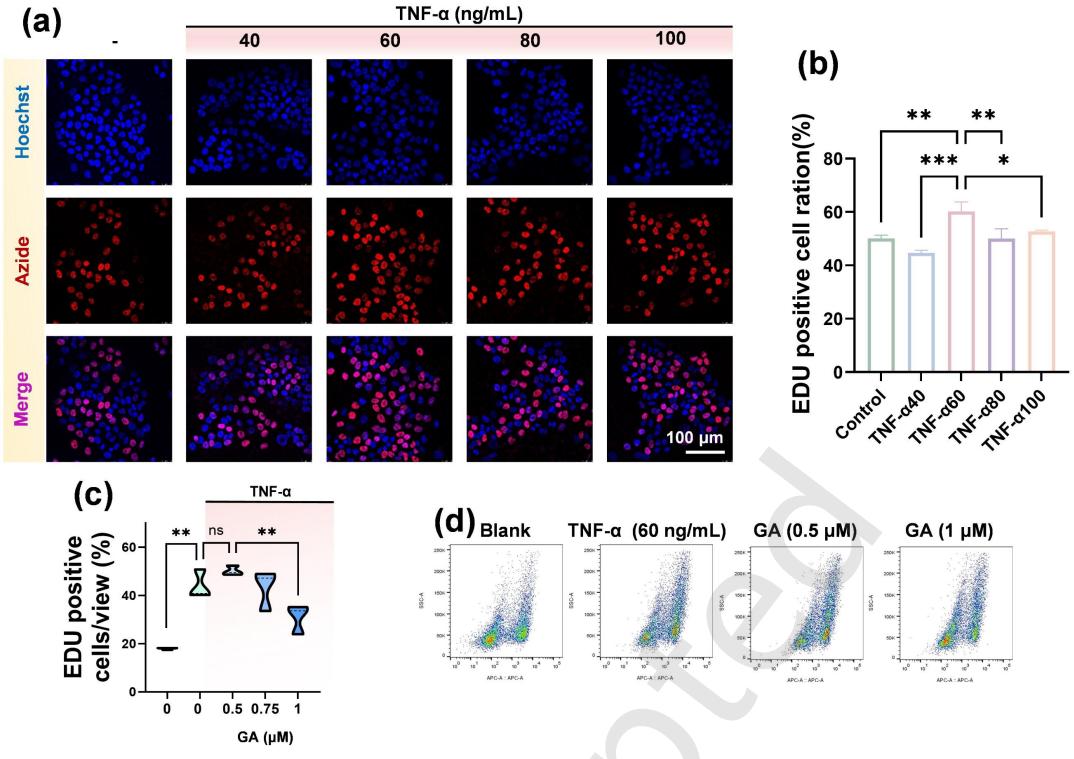


Figure S1 TNF-α induced abnormal proliferation of HaCaT cells. (a) Confocal micrograph of different concentrations of TNF-α inducing abnormal proliferation of HaCaT cells. (b) Statistical graph of abnormal proliferation of HaCaT cells induced by different concentrations of TNF-α. (c-d) Flow cytometry analysis of GA-mediated inhibition of TNF-α-induced HaCaT cell proliferation after indicated treatments. All statistical data are presented as mean ± SD, n = 3. *p < 0.05, **p < 0.01, ***p < 0.001. Scale bars, 100 μm.

Just Accepted

Address correspondence to Mengnan Zhao, zhaomengnan@cdutcm.edu.cn

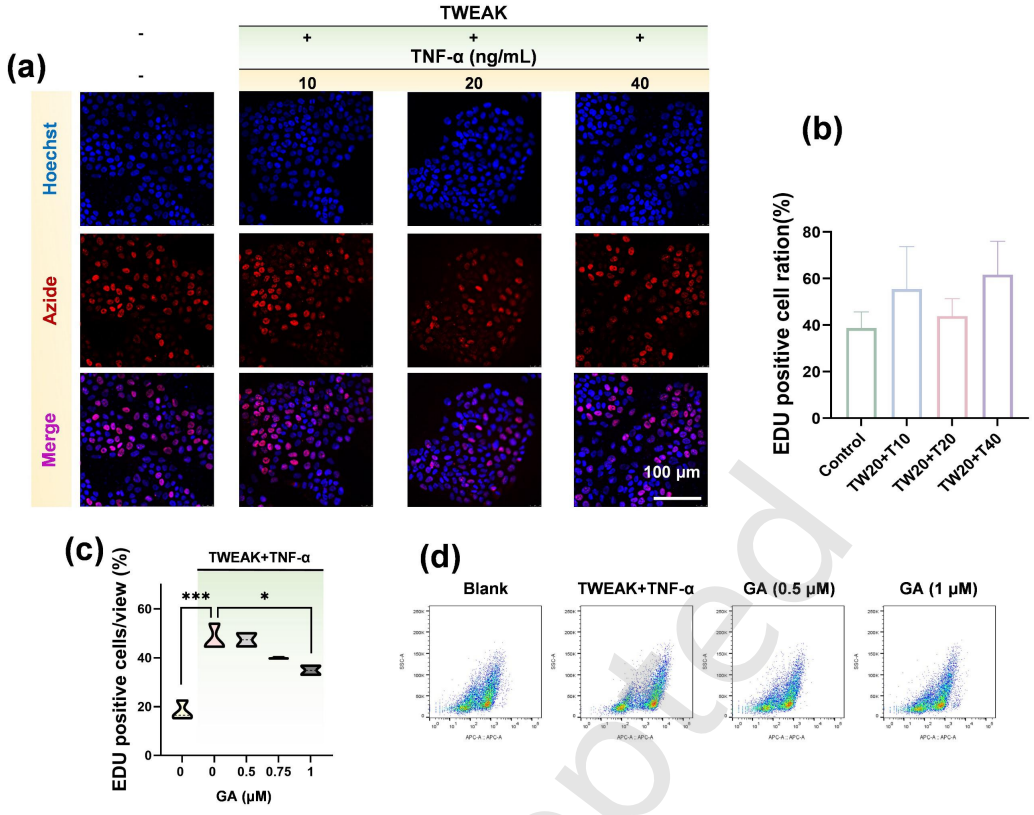


Figure S2 TWEAK and TNF-α induced abnormal proliferation of HaCaT cells. (a) Confocal microscopy graph of abnormal proliferation of HaCaT cells induced by the action of TWEAK and different concentrations of TNF-α for 48 h. (b) Statistical graph of TWEAK and TNF-α induced abnormal proliferation data of HaCaT cells. (c-d) Flow cytometry analysis of GA-inhibited proliferation in HaCaT cells induced by TWEAK and TNF-α. All statistical data are presented as mean ± SD, n = 3. Scale bars, 100 μm.

Just Accepted

Address correspondence to Mengnan Zhao, zhaomengnan@cdutcm.edu.cn

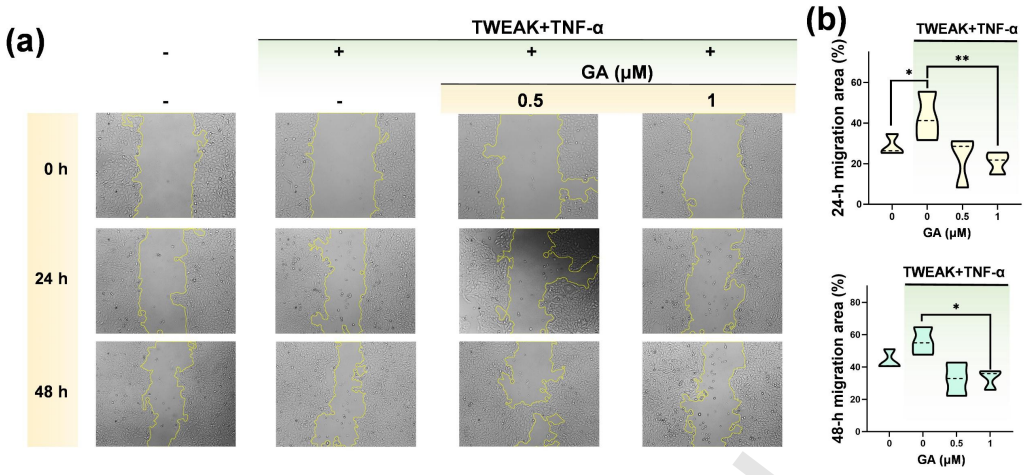


Figure S3 (a) GA inhibits the accelerated scratch wound healing closure co-induced by TWEAK and TNF-α in HaCaT cells. (b) Quantitative analysis of scratch wound healing rates after indicated treatments at 24 and 48 h. All statistical data are presented as mean ± SD, n = 3. *p < 0.05, **p < 0.01. Scale bar, 100 μm.

Just Accepted

Address correspondence to Mengnan Zhao, zhaomengnan@cdutcm.edu.cn

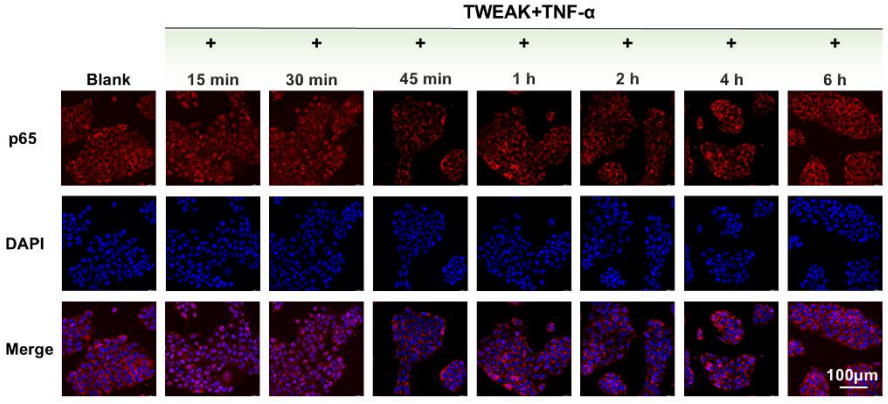


Figure S4 TWEAK and TNF-α stimulate p65 nuclear translocation. 20 ng/mL TWEAK and 10 ng/mL TNF-α stimulate p65 nuclear translocation at different times. All statistical data are presented as mean ± SD, n = 3. Scale bars, 100 μm.

Just Accepted

Address correspondence to Mengnan Zhao, zhaomengnan@cdutcm.edu.cn

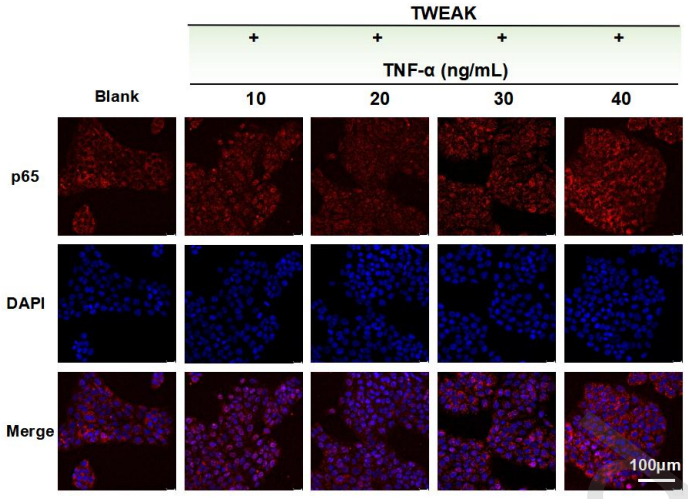


Figure S5 TWEAK and TNF-α induced p65 nuclear translocation. 20 ng/mL TWEAK and different concentrations of TNF-α for 30 min induced p65 nuclear translocation of HaCaT cells. All statistical data are presented as mean ± SD, n = 3. Scale bar, 100 μm.

Just Accepted

Address correspondence to Mengnan Zhao, zhaomengnan@cdutcm.edu.cn

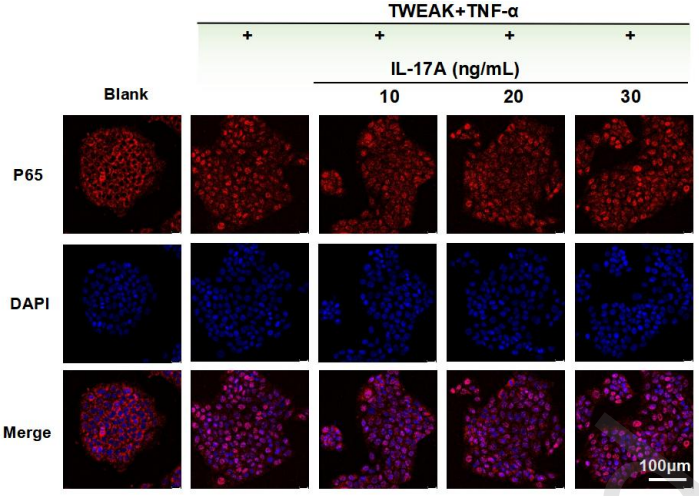


Figure S6 TWEAK, TNF-α and IL-17A together induced abnormal proliferation of HaCaT cells. Abnormal proliferation of HaCaT cells was induced by 20 ng/ml TWEAK, 10 ng/ml TNF-α and different concentrations of IL-17A for 30 min. All statistical data are presented as mean ± SD, n = 3. Scale bars, 100 μm.

Just Accepted

Address correspondence to Mengnan Zhao, zhaomengnan@cdutcm.edu.cn

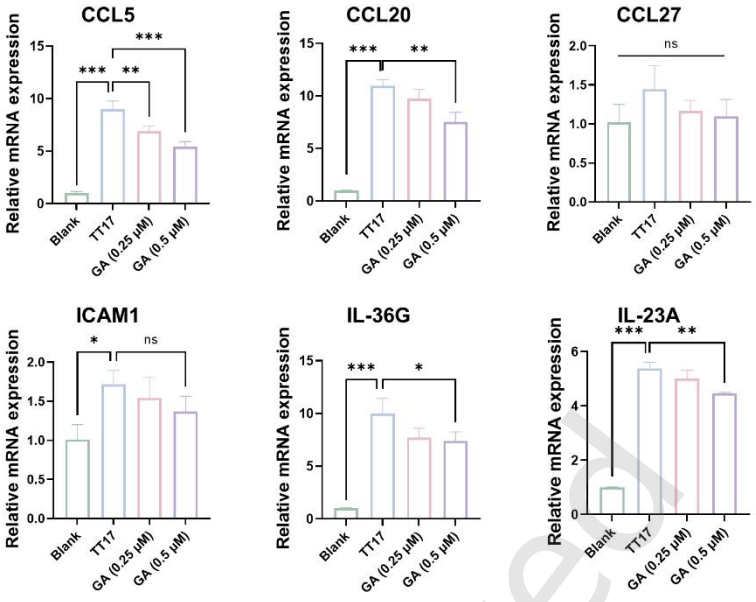


Figure S7 Effect of GA on the relative gene expression of CCL5, CCL20, CCL27, ICAM1, IL36G, and IL23A induced by TWEAK, TNF-α, and IL-17A. Gene expression was normalized to GAPDH. All statistical data are presented as mean ± SD, n = 3. *p < 0.05, **p < 0.01, ***p < 0.001.

Just Accepted

Address correspondence to Mengnan Zhao, zhaomengnan@cdutcm.edu.cn

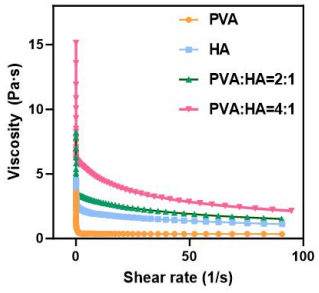


Figure S8 Rheological properties (viscosity vs. shear rate) of the varying microneedle matrix solutions.

Just Accepted

Address correspondence to Mengnan Zhao, zhaomengnan@cdutcm.edu.cn

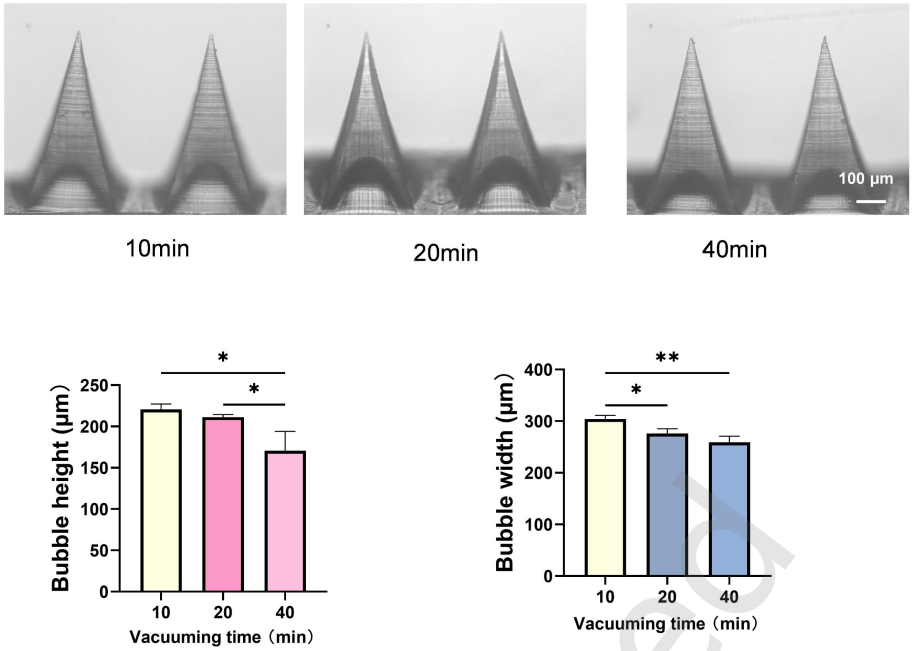


Figure S9 Characterization of PVA/HA air-bubble microneedles at a PVA-to-HA ratio of 4:1. Bubble height and width under different evacuation times. All statistical data are presented as mean ± SD, n = 3. *p < 0.05, **p < 0.01, ***p < 0.001.

Just Accepted

Address correspondence to Mengnan Zhao, zhaomengnan@cdutcm.edu.cn

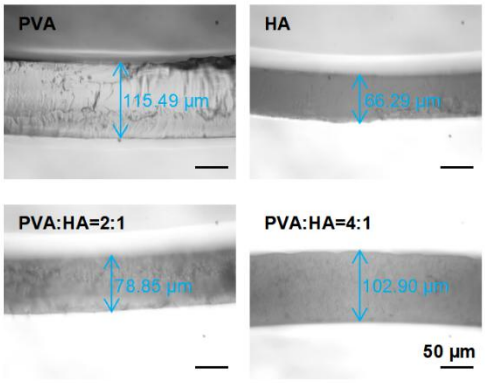


Figure S10 Photographs of dried film thickness from equal-volume PVA, HA, and PVA/HA solutions at various ratios.

Just Accepted

Address correspondence to Mengnan Zhao, zhaomengnan@cdutcm.edu.cn

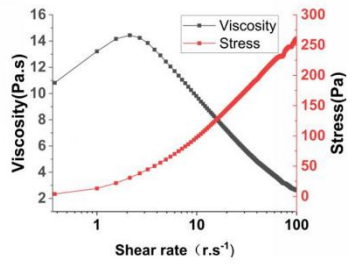


Figure S11 Characterization of PVA/HA air bubble MNs. Rheological behavior of microneedle matrix solutions: shear stress and viscosity as a function of shear rate.

Just Accepted

Address correspondence to Mengnan Zhao, zhaomengnan@cdutcm.edu.cn

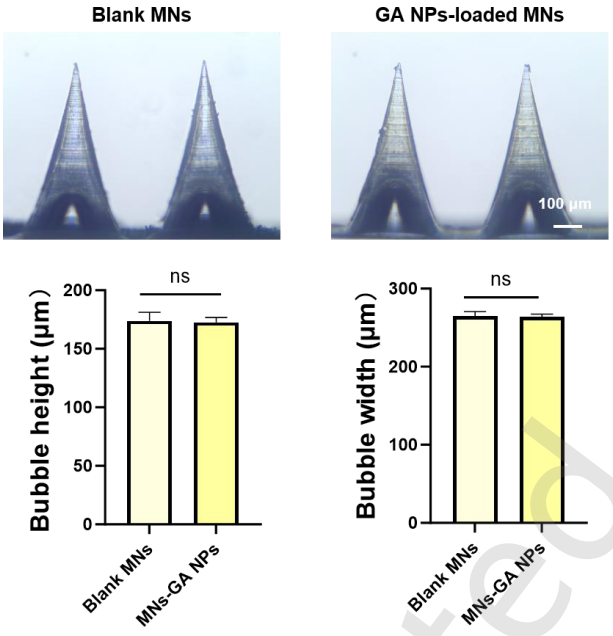


Figure S12. Bubble size (height and width) of blank MNs and GA NPs-loaded MNs. All statistical data are presented as mean ± SD, *n* = 3.

Just Accepted

Address correspondence to Mengnan Zhao, zhaomengnan@cdutcm.edu.cn

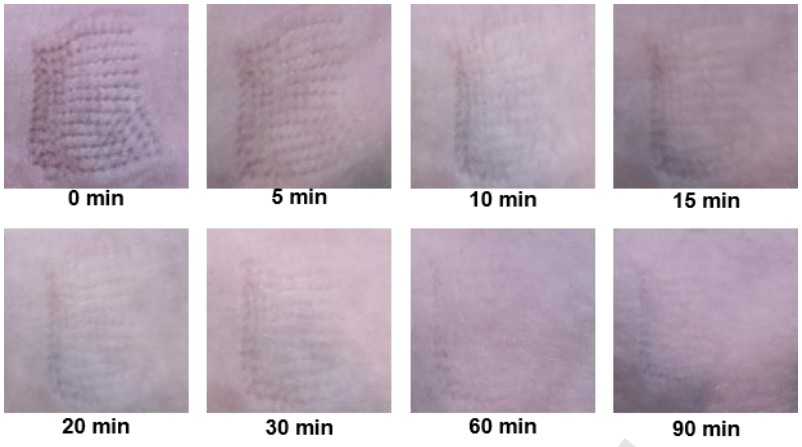


Figure S13 Recovery of skin tissue following microneedle administration.

Just Accepted

Address correspondence to Mengnan Zhao, zhaomengnan@cdutcm.edu.cn

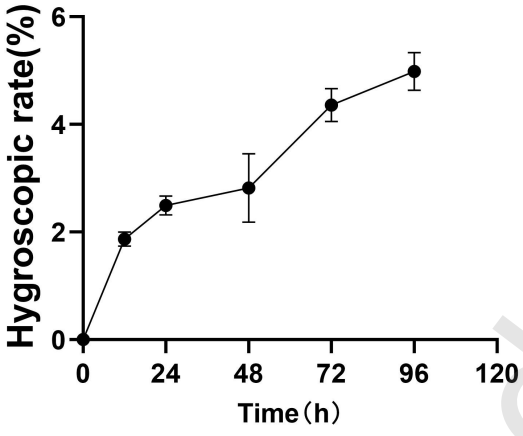


Figure S14. Moisture absorption capacity of the microneedle patch. All statistical data are presented as mean ± SD, n = 3.

Just Accepted

Address correspondence to Mengnan Zhao, zhaomengnan@cdutcm.edu.cn

Table S1 Physico-chemical characterization of nanoparticles (n = 3, mean ± SD).

Encapsulation efficiency (%)	drug loading (%)	Size (nm)	zeta potential (mV)	PDI
79.65 ± 0.44	19.91 ± 0.11	141.81 ± 6.5	-6.35 ± 0.46	0.29 ± 0.06

Just Accepted

Address correspondence to Mengnan Zhao, zhaomengnan@cdutcm.edu.cn

Table S2 Primer sequences used for quantitative PCR analysis of human genes.

Gene	Forward primer (5'-3')	Reverse primer (5'-3')
GADPH	ATTCCACCCATGGCAAATTCC	GCATCGCCCCACTTGATTTT
CCL5	GGACACCACACCCTGCTGCTTTG	ACACACTTGGCGGTTCTTTCGGG
CCL20	TACTCCACCTCTGCGGCGAATCAGAA	GTGAAACCTCCAACCCCAGCAAGGTT
CCL27	AAAGCTCCATGGGACTCTGC	TTGGCTATTGGGGGCTTCAG
ICAM1	GGCTGGAGCTGTTTGAGAAC	ACTGTGGGGTTCAACCTCTG
IL-36G	CTGGAGCCACGATTCAGTCC	AGGGTCCACACTTGCTGATTC
IL-23A	CTTTCACAGAAGCTCTGCACAC	GCAAGCAGAACTGACTGTTGTC

Table S3 Primer sequences used for quantitative PCR analysis of mouse genes.

Gene	Forward primer (5'-3')	Reverse primer (5'-3')
Gapdh	AAGAAGGTGGTGAAGCAGG	GAAGGTGGAAGAGTGGGAG
Il-1β	GCCACCTTTTGACAGTGATGAG	CTGCCTGAAGCTCTTGTTGATG
Il-6	TCCATCCAGTTGCCTTCTTGG	CCACGATTTCCCAGAGAACATG
iNOS	CCTGCTTTGTGCGAAGTGTC	CCCAAACACCAAGCTCATGC
Il-17a	ACCGCAATGAAGACCCTGATAG	AGCATCTTCTCGACCCTGAAAG
Il-23a	TGAAGGGCAAGGACACCATTAT	TTCTCACAGTTTCTCGATGCCA
Ccl5	ATGGCTCGGACACCACTCCCTG	GGTTGGCACACACTTGGCGGTT
Ccl20	TGGGTTTCACAAGACAGATGG	TGAGGAGGTTCACAGCCCTT

Just Accepted

Address correspondence to Mengnan Zhao, zhaomengnan@cdutcm.edu.cn